Maximum-Likelihood Retrieval of Volcanic Ash Concentration and Particle Size From Ground-Based Scanning Lidar

Luigi Mereu, Simona Scollo, Saverio Mori, *Member, IEEE*, Antonella Boselli, Giuseppe Leto, and Frank S. Marzano, *Fellow, IEEE*

***Abstract*— An inversion methodology, named maximum-likelihood (ML) volcanic ash light detection and ranging (Lidar) retrieval (VALR-ML), has been developed and applied to estimate volcanic ash particle size and ash mass concentration within volcanic plumes. Both estimations are based on the ML approach, trained by a polarimetric backscattering forward model coupled with a Monte Carlo ash microphysical model. The VALR-ML approach is applied to Lidar backscattering and depolarization profiles, measured at visible wavelength during two eruptions of Mt. Etna, Catania, Italy, in 2010 and 2011. The results are compared with those of ash products derived from other parametric retrieval algorithms. A detailed comparison among these different retrieval techniques highlights the potential of VALR-ML to determine, on the basis of a physically consistent approach, the ash cloud area that must be interdicted to flight operations. Moreover, the results confirm the usefulness of operating scanning Lidars near active volcanic vents.**

***Index Terms*— Ash mean size, backscattering and depolarization, explosive eruption, retrieval algorithms, scanning light detection and ranging (Lidar), volcanic ash concentration.**

I. Introduction

An EXPLOSIVE volcanic eruption can cause a variety of severe and widespread threats to human well-being and the environment [1], [3], [12]. The ash produced during explosive eruptions has a huge impact on the global environment. Major eruptions strongly influence the earth's radiative balance by injecting into the atmosphere a large quantity of particles and gases, which produce secondary aerosols [18]. Although the concentration of stratospheric volcanic aerosols is usually very low and rare, they can have notable impact on global climate due to their large-scale dispersion and residence times in the order of months or even several years. By contrast, the residence time of volcanic aerosols in the troposphere is only in the order of several days or months depending on the eruption intensity and duration. Furthermore, its spatial distribution can be rather inhomogeneous affected mainly by the eruption and atmospheric variability, so that the assessment of their radiative effects is much more complicated [10]. Volcanic ash is critical information for the flight safety of jet-driven aircrafts. Indeed, due to their low melting temperature and their sharp-edged shapes, ash particles can severely damage the turbines and again here and front windows of aircraft [2], [4], [21], [29]. The ash concentration in the atmosphere is an important parameter that needs to be detected with some accuracy [42], because air traffic must be suspended in the regions in which volcanic ash concentrations exceed certain thresholds [10], [11].

In recent years, light detection and ranging (Lidar) systems have been widely used to study volcanic aerosol clouds produced by major volcanic eruptions [22]. Lidar techniques are a powerful method for monitoring the dispersion of a volcanic cloud in the atmosphere because of their profiling capability at very high range resolution. A Lidar can measure not only backscatter but also depolarization once two-way path attenuation is properly corrected. Lidar observations can provide plume geometrical properties (i.e., top, bottom, and thickness), its optical depth, aerosol category, and also aerosol microphysical properties if advanced multiwavelength Raman Lidar systems are used [45]. Using the depolarization channel, it is also possible to distinguish various shapes of ash particles [10], [12].

The capability of Lidar systems to detect the finest particles in volcanic plume and reliably estimate the ash concentration mainly depends on instrumental characteristics and the type of explosive activity. For typical ground-based dual-polarized Lidars, the evaluation of the aerosol backscattering and depolarization coefficients may be carried out only in those regions where the Lidar signal is not extinguished inside the volcanic plume optical thickness. In these cases, assuming the knowledge of the Lidar ratio (LR) between extinction and backscattering, path attenuation correction algorithms can be applied to reconstruct the effective Lidar observable [22].

Manuscript received July 26, 2017; revised January 22, 2018; accepted March 15, 2018. Date of publication May 21, 2018; date of current version September 25, 2018. This work was supported in part by the European FP7 Project APHORISM (FP7–SPA-2013) under Grant 606738 and in part by H2020 Project EUROVOLC (call H2020-INFRAIA-2017-1) under Grant 731070-2. *(Corresponding author: Luigi Mereu.)*

L. Mereu, S. Mori, and F. S. Marzano are with the Dipartimento di Ingegneria dell'Informazione, Sapienza Università di Rome, 00184 Rome, Italy, and also with the CETEMPS Center of Excellence, Università dell'Aquila, 67100 L'Aquila, Italy (e-mail: mereu@diet.uniroma1.it; mori@diet.uniroma1.it; marzano@diet.uniroma1.it).

S. Scollo is with the Istituto Nazionale di Geofisica e Vulcanologia, Osservatorio Etneo, Sezione di Catania, 95125 Catania, Italy (e-mail: simona.scollo@ingv.it).

A. Boselli is with the Istituto di Metodologie per l'Analisi Ambientale, Consiglio Nazionale delle Ricerche, 85055 Potenza, Italy (e-mail: antonella.boselli@imaa.cnr.it).

G. Leto is with the Istituto Nazionale di Astrofisica, Osservatorio Astrofisico di Catania, 95123 Catania, Italy, (e-mail: gle@oact.inaf.it).

This paper has supplementary downloadable material available at http://ieeexplore.ieee.org, provided by the author.

Color versions of one or more of the figures in this paper are available online at http://ieeexplore.ieee.org.

Digital Object Identifier 10.1109/TGRS.2018.2826839

Optically thick plumes can strongly attenuate the Lidar beam, reducing its penetration capability due to absorption effects. Inversion approaches can mitigate the effect of path attenuation by reconstructing the backscatter profile if the return signal is detectable [7], [15]. On the other hand, Lidar beam divergence is generally very small (about a few m^3 at ranges of tens of kilometer) so that they can have a better spatial resolution than that of a radar microwave system, even though at the expense of a smaller wide-area search capability. Multiple scattering (MS) is a further effect that can impact the ash retrieval due to the apparent increase of the return power [46], [47]. However, for relatively low attenuation and/or highly directive lasers close to the explosive volcanic source, the MS tends to be negligible.

Lidar sensors with scanning capability, installed a few kilometers away from the summit craters, can be valid supports in monitoring the finest airborne ash particles that are rapidly dispersed by the prevailing wind. Lidar measurements near an active volcano are crucial for continuous monitoring of long-lived explosive activity and improving the volcanic ash plume forecast during volcanic crises; nevertheless, Lidar systems can be seriously damaged by ash fallout if not properly protected. The measurements near Etna volcano in Italy, one of the most active volcanoes on the earth, were performed with the volcanic ash monitoring by polarization (VAMP) Lidar [43]. The VAMP system is a portable dual-polarized Lidars with scanning capabilities, allowing detecting elastic backscattered radiation at 532 nm [22]. This system is able to provide highly accurate measurements of the backscatter coefficient and low depolarization ratio with a range resolution of 60 m and an azimuth resolution of 1°. Whereas water clouds and fog contain spherical liquid droplets exhibiting low aersosol depolarization values, volcanic ash particles are generally asymmetrical associated with high aerosol depolarization values. The latter is readily detected by the VAMP system thanks to its dual polarization channels. Some recent eruptions of Etna volcano were extensively observed by the VAMP system. The calibration of the VAMP system and a detailed description of the apparatus are reported in [22] and [32]. These observations have opened the possibility to validate the scanning mode of Lidar instruments and, now, to test different retrieval approaches of ash properties.

The main goals of this paper are as follows.

1) To introduce the maximum-likelihood (ML) volcanic ash Lidar retrieval (VALR-ML) based on a Monte Carlo microphysically oriented backscattering polarimetric forward model. The overall numerical model, called hydrometeor-ash particle ensemble scattering simulator (HAPESS), takes into account the physical and electromagnetic behavior of ash particle polydispersions in a statistical way.
2) To apply the VALR-ML algorithm to the VAMP data collected during two different explosive events of Etna volcano: a prolonged ash emission activity occurring in 2010 at the North East Crater and during a lava fountain in 2011 at the New South East Crater. The VALR-ML algorithm results are compared with those of ash concentration estimations, obtained from a parametric retrieval model to evaluate the impact of choosing different approaches for ash-mass no-flight zone contouring [22], [30], [33].

This paper is organized as follows. Section II illustrates the Lidar polarimetric data processing technique, focusing on the numerical forward model, simulation of Lidar observables (also reported in the Appendix) and ML retrieval methodology. Section III focuses on the application of VALR-ML to the two Etna eruptions in 2010 and 2011 and on the comparison of results with those obtained by other parametric retrieval algorithms. Section IV draws the conclusion and sets out future work.

II. Polarimetric Lidar Data Processing

The physical approach to Lidar remote sensing requires developing a microphysical model that takes into account the volcanic particles features (size, density, shape, and refractivity) and its associated backscattering polarimetric response. This forward model can then be used to approach the inverse problem by training an estimation algorithm by means of a set of realistic randomly generated simulations of the forward model itself. This physical–statistical approach should tackle the issues of nonuniqueness and uncertainty, which affect any remote sensing problem.

A. Volcanic Particle Lidar Model

The microphysical–electromagnetic forward model summarizes the ash particle features, derived from available experimental data and considered as *a priori* information to constrain the inverse solution [35]. The main microphysical properties of ash particle useful for modeling are as follows:

1) particle size distribution (PSD);
2) density;
3) angular orientation;
4) axial ratio in case of spheroidal shapes;
5) relative dielectric constant models for the frequency/wavelength of interest [16].

The optical Lidar response is mainly determined by the PSD of each microphysical species within the detected range volume. The PSD is usually modeled through either a normalized Gamma or Weibull size distribution. In the case of a multimode size distribution, it is always possible to suppose more than one analytical PSD characterized by different mean sizes and total number of particles. We adopt the scaled-gamma (SG) PSD as a general model for both ash and hydrometeor particles modeled as a polydispersion of randomly oriented spheroidal particles [17]. If r is the radius of a volume-equivalent spherical particle (SP) (i.e., a sphere whose volume is equivalent to the associated spheroidal particle), the SG PSD N_p, for a generic class of ash particles p, can be written as

$$N_p(r) = N_{\mathrm{np}} \left(\frac{r}{r_{\mathrm{np}}}\right)^{\mu_p} e^{-\Lambda_{\mathrm{np}}\left(\frac{r}{r_{\mathrm{np}}}\right)} \tag{1}$$

where r_{np} is the number-weighted mean radius, whereas the "intercept" parameter N_{np} and the "slope" parameter Λ_{np} in a logarithmic plane are related to the "shape" parameter μ_p

and to the particle density ρ_p, as in [47]. If particles are volume-equivalent spheres, their mass is $m_p = \rho_p \cdot (4\pi/3) \cdot r^3$ with a constant density ρ_p; the minimum and maximum radius are 0 and infinite so that the complete moment m_{np} of order n of N_p can be expressed by

$$m_{\text{np}} = \frac{N_{\text{np}}(2r_{\text{np}})^{n+1}}{\Lambda_{\text{np}}^{n+\mu_p+1}}\Gamma(n+\mu_p+1) \tag{2}$$

where $\Gamma\ (n+1) = n!$ if n is an integer. Using (2), the total volumetric number of particles N_{tp} [m^{-3}] is $N_{\text{tp}} = m_{0p}$, whereas the mass concentration C_p [mg/m^3] is given by $C_p = \pi/6 \cdot \rho_p \cdot m_{3p}$ and the number-weighted particle mean radius r_{np} [μm] is defined by $r_{\text{mp}} = m_{1p}/m_{0p}$

$$\begin{cases} C_p = \displaystyle\int_0^\infty \frac{4}{3}\pi r^3 \rho_p(r) N_p(r) dr = \frac{4}{3}\pi \rho_p m_3 \\ r_{\text{np}} = \dfrac{\int_0^\infty r N(r) dr}{\int_0^\infty N(r) dr} = \dfrac{m_1}{m_0} = \dfrac{D_{\text{np}}}{2} \end{cases} \tag{3a}$$

where

$$r_{\text{ep}} = \frac{\int_0^\infty r^3 N_p(r) dr}{\int_0^\infty r^2 N_p(r) dr} = \frac{m_3}{m_2} = \left(\frac{m_3}{m_2}\frac{m_0}{m_1}\right) r_{np} \tag{3b}$$

where r_{ep} being the effective radius [μm], expressed as a ratio between the third and second moments of N_p, proportional to the number-weighted particle mean radius r_{np} and its associated mean diameter D_{np}.

For general purposes, we can define a number of ash classes with respect to their average size. It is worth noting that the following size discrimination differs to the one usually adopted by volcanologists [25], [37]. The following ash-diameter classes are identified (as integer powers of 2):

1) very fine ash (VA) with mean equivalent diameters between 2^{-3} and 2^3 μm;
2) fine ash (FA) between 2^3 and 2^6 μm;
3) coarse ash (CA) between 2^6 and 2^9 μm;
4) small lapilli (SL) between 2^9 and 2^{12} μm;
5) large lapilli (LL) between 2^{12} and 2^{15} μm.

Each diameter class may be subdivided with respect to other main parameters, e.g., the ash concentration, orientation angle, and axis ratio. The model of ash particle properties is completed by considering the following sets of ash subclasses, listed in Table I:

1) five classes for four different ash concentrations (i.e., very small = VC, small = SC, moderate = MC, intense = IC, and uniform = UC, where the latter includes all previous ones);
2) five classes for five different orientations (i.e., tumbling with $\theta = 30° =$ TO.1, tumbling with $\theta = 45° =$ TO.2, tumbling with $\theta = 60° =$ TO.3, oblate = OO, and prolate = PO);
3) five classes for two different axis ratio models (RB: ratio basaltic–andesitic and RR: ratio rhyolitic), even though we have here selected only the RB case considering the particle features from Etna (see also [6], [17]).

Considering all combinations, we can obtain subclasses for each size class. In general, we can list $5 \times 4 \times 5 \times 2 = 200$ subclasses if VC, SC, MC, and IC are considered and $5 \times 1 \times 5 \times 2 = 50$ subclasses if UC is considered. *A priori* information about the volcanic scenario allows tailoring the overall simulations data set in terms of contributing subclasses.

The goal, as mentioned, is to build a data set of simulated Lidar observables, obtained with a Monte Carlo random generation of ash particle ensembles following the statistics of their main descriptive parameters. The minimum significant number of ash parameters, identified for our purposes, is given in Table I and listed as follows:

1) PSD mean equivalent radius r_e;
2) mass concentration C_p;
3) PSD shape parameter μ_p;
4) particle density ρ_p;
5) mean canting angle m_θ of the particle orientation distribution (POD) $p_p(\theta)$;
6) POD canting angle standard deviation σ_θ;
7) axial ratio ρ_{ax};
8) dielectric constant with an SiO_2 weight W_{SiO2} dependence for the real and imaginary parts and relative humidity fraction.

Table I summarizes the range of values for each parameter, either derived from [6], [23], and [44] or determined heuristically [1]. Supplementary information, sketched in Table I, is also described in [16].

The Lidar backscattering coefficients β_{hh}, β_{vv}, and β_{vh} at horizontal (h) and vertical (v) polarization states can be written in terms of the scattering matrix elements S_{xy} and PSD N_p, as

$$\begin{aligned} \beta_{xy}(\lambda) &= \int_0^\pi \int_0^\infty 4\pi \left|S_{xy}^{(b)}(r,\theta,\lambda)\right|^2 N_p(r) \\ p_p(\theta) dr \sin\theta d\theta &= \left\langle 4\pi S_{xy}^{(b)}(r,\theta,\lambda)\right\rangle \end{aligned} \tag{4}$$

where $x = h, v$ again stands for the receiving mode and $y = h, v$ for the transmitting mode polarization. Note that β_{xy} is usually expressed in [km^{-1} · sr^{-1}]. Considering that β_{xy} can go typically from 10^{-6} up to 10^{-3} km^{-1} · sr^{-1}, here we prefer to express β_{xy} in dBβ, that is, a value in decibel equals $10 \cdot \log_{10}(\beta_{xy})$ when β_{xy} is expressed in [m^{-1} · sr^{-1}], in analogy to radar meteorology where dBZ is widely used. This means that typical values of backscatter will go from -60 up to -30 dBβ. Note that for completeness, in the Appendix, expressions of Lidar polarimetric observables are also given in terms of the Stokes vectors and the scattering phase (Muller) matrix in order to show the parallelism of definitions for both Lidar and radar applications.

The specific attenuation or extinction coefficient α_{xy} is expressed in [km^{-1}] and is defined as

$$\alpha_{xy}(\lambda) = 2\lambda \text{Im}\left\{4\pi S_{xy}^{(b)}(r,\varphi,\lambda)\right\}. \tag{5}$$

Similar to (4), if α_{xy} is in [km^{-1}], $\alpha_{XY} = 4.343 \cdot \alpha_{xy}$ is conventionally expressed in dB/km. The Lidar linear co-polarization and cross-polarization (adimensional) ratios are defined, respectively, by

$$\delta_{\text{co}} = \frac{\beta_{\text{vv}}(\lambda) - \beta_{\text{hh}}(\lambda)}{\beta_{\text{vv}}(\lambda) + \beta_{\text{hh}}(\lambda)} \tag{6}$$

$$\delta_{\text{cr}} = \frac{\beta_{\text{vh}}(\lambda)}{\beta_{\text{hh}}(\lambda)}. \tag{7}$$

TABLE I

OVERVIEW OF SUPERVISED ASH CLASS PARAMETERIZATION WITH THE LIST OF THE MAIN VARIABLES AND THEIR ASSUMED STATISTICAL CHARACTERIZATION EITHER DERIVED FROM THE LITERATURE OR HEURISTICALLY DETERMINED. NOTE THAT PDF STANDS FOR PROBABILITY DENSITY FUNCTION (U: UNIFORM), PSD FOR PARTICLE SIZE DISTRIBUTION, Δx FOR RANGE VARIABILITY OF x PARAMETER, m_x FOR MEAN OF x AND σ_x FOR STANDARD DEVIATION OF x, AND AR FOR PARTICLE ASPECT RATIO (SEE [17] FOR DETAILS)

Ash Particle Ensemble Property	***Very Fine Ash (VA)***	***Fine Ash (FA)***	***Coarse Ash (CA)***	***Small Lapilli (SL)***	***Large Lapilli (LL)***
Ash diameter **Variability range** ΔD_n (μm)	*Uniform PDF* ΔD_n 2^{-3}-2^{3} 0.125-8	*Uniform PDF* ΔD_n 2^{3}-2^{6} 8-64	*Uniform PDF* ΔD_n 2^{6}-2^{9} *64-512*	*Uniform PDF* ΔD_n 2^{9}-2^{12} 512-4096	*Uniform PDF* ΔD_n 2^{12}-2^{15} 4096-32768
Ash particle concentration **Variability range** UC**:** ΔC_p (mg/m^3) VC: Very Small Conc. SC: Small Conc. MC: Medium Conc. IC: Intense Conc.	*Uniform PDF* ΔC_p =10^{-3}-10^{4} VC: 10^{-3}-10^{0} SC: 10^{0}-10^{2} MC: 10^{2}-10^{3} IC: 10^{3}-10^{4}	*Uniform PDF* ΔC_p =10^{-3}-10^{4} VC: 10^{-3}-10^{0} SC: 10^{0}-10^{2} MC: 10^{2}-10^{3} IC: 10^{3}-10^{4}	*Uniform PDF* ΔC_p =10^{-3}-10^{4} VC: 10^{-3}-10^{0} SC: 10^{0}-10^{2} MC: 10^{2}-10^{3} IC: 10^{3}-10^{4}	*Uniform PDF* ΔC_p =10^{-3}-10^{4} VC: 10^{-3}-10^{0} SC: 10^{0}-10^{2} MC: 10^{2}-10^{3} IC: 10^{3}-10^{4}	*Uniform PDF* ΔC_p =10^{-3}-10^{4} VC: 10^{-3}-10^{0} C: 10^{0}-10^{2} MC: 10^{2}-10^{3} IC: 10^{3}-10^{4}
Ash size distribution shape parameter μ_p (adimensional)	*Scaled Gamma PSD* μ_p = 1-2 *U-PDF*	*Scaled Gamma PSD* μ_p = 1-2 *U-PDF*	*Scaled Gamma PSD* μ_p = 1-2 *U-PDF*	*Scaled Gamma PSD* μ_p = 1-2 *U-PDF*	*Scaled Gamma PSD* μ_p = 1-2 *U-PDF*
Ash particle density ρ_p (g/cm^3)	*Uniform PDF* ρ_p = 0.5-2.5	*Uniform PDF* ρ_p = 0.5-2.5	*Uniform PDF* ρ_p = 0.5-2.5	*Uniform PDF* ρ_p = 0.5-2.5	*Uniform PDF* ρ_p = 0.5-2.5
Ash particle canting angle mean and deviation m_f (°) and σ_f (°) *TO.1: Tumbling Orientation,* *TO.2: Tumbling Orientation,* *TO.3: Tumbling Orientation,* *OO: Oblate Orientation* *PO : Prolate Orientation*	*TO.1: G-PDF* m_ϕ=30°;σ_ϕ=30° *TO.2: G-PDF* μ_ϕ=45°;σ_ϕ=30° *TO.3: G-PDF* μ_ϕ=60°;σ_ϕ=30° *OO: G-PDF* μ_ϕ=0°;σ_ϕ=10° *PO: G-PDF* μ_ϕ= 90°; σ_ϕ=10°	*TO.1: G-PDF* m_ϕ=30°; σ_ϕ=30° *TO.2: G-PDF* μ_ϕ=45°; σ_ϕ=30° *TO.3: G-PDF* μ_ϕ=60°; σ_ϕ=30° *OO: G-PDF* μ_ϕ=0°; σ_ϕ=10° *PO: G-PDF* μ_ϕ= 90°; σ_ϕ=10°	*TO.1: G-PDF* μ_ϕ=30°; σ_ϕ=30° *TO.2: G-PDF* μ_ϕ=45°; σ_ϕ=30° *TO.3: G-PDF* μ_ϕ=60°; σ_ϕ=30° *OO: G-PDF* μ_ϕ=0°; σ_ϕ=10° *PO: G-PDF* μ_ϕ= 90°; σ_ϕ=10°	*TO.1: G-PDF* μ_ϕ=30°; σ_ϕ=30° *TO.2: G-PDF* μ_ϕ=45°; σ_ϕ=30° *TO.3: G-PDF* μ_ϕ=60°; σ_ϕ=30° *OO: G-PDF* μ_ϕ=0°; σ_ϕ=10° *PO: G-PDF* μ_ϕ= 90°; σ_ϕ=10°	*TO.1: G-PDF* μ_ϕ=30°; σ_ϕ=30° *TO.2: G-PDF* μ_ϕ=45°; σ_ϕ=30° *TO.3: G-PDF* μ_ϕ=60°; σ_ϕ=30° *OO: G-PDF* μ_ϕ=0°; σ_ϕ=10° *PO: G-PDF* μ_ϕ= 90°; σ_ϕ=10°
Non-spherical particle axial ratio r_{ax} : axis ratio [adim] RB: basaltic ratio RR: rhyolitic ratio	r_{ax}=AR RB: $r_{ax\text{-}b}$ RR: $r_{ax\text{-}r}$	r_{ax}=AR RB: $r_{ax\text{-}b}$ RR: $r_{ax\text{-}r}$	r_{ax}=AR RB: $r_{ax\text{-}b}$ RR: $r_{ax\text{-}r}$	r_{ax}=AR RB: r_{ax} =1.4 RR: r_{ax} =2.4	r_{ax}=AR RB: r_{ax} =1.4 RR: r_{ax} =2.4
Optical dielectric constant for volcanic ash	*Uniform PDF*	*Uniform PDF*	*Uniform PDF*	*Uniform PDF*	*Uniform PDF*

Typically, for a Lidar system, other parameters are also defined, such as the extinction to backscatter LidarLR [sr]

$$R_{\beta\alpha x}(\lambda) = \frac{\alpha_{xx}(\lambda)}{\beta_{xx}(\lambda)}. \tag{8}$$

If the extinction coefficients at two wavelengths λ_1 and λ_2 are known, the extinction Angström coefficient (unitless) can be determined by

$$A_{\alpha x}(\lambda_1/\lambda_2) = -\frac{\ln[\alpha_{xx}(\lambda_1)/\alpha_{xx}(\lambda_2)]}{\ln\left(\frac{\lambda_1}{\lambda_2}\right)} \tag{9}$$

where $\lambda_1 < \lambda_2$. Similarly, we can define the backscatter-related Angström coefficient (unitless) through

$$A_{\beta x}(\lambda_1/\lambda_2) = -\frac{\ln[\beta_{xx}(\lambda_1)/\beta_{xx}(\lambda_2)]}{\ln\left(\frac{\lambda_1}{\lambda_2}\right)} \tag{10}$$

where β_{xx} replaces α_{xx} in (9).

In order to compute the Lidar observables in (4)–(10), the nonsphericity of ash particles is considered by assuming spheroids. The particle scattering and absorption properties are computed using the T-matrix method, supplemented by the geometrical optics approach in the optical scattering regime where T-matrix is subject to numerical convergence problems. The T-matrix method has been widely applied to studying nonabsorbing and non-SPs in the visible and infrared spectral regions [20], [50]. The VALR algorithm can also include the ash–hydrometeor mixed and coexisting classes, in principle, by combining ash and hydrometeor modeling. Hydrometeor scattering and modeling is well described elsewhere. Any advancement in the understanding of the observed ash clouds can be, in principle, incorporated within the forward model HAPESS in order to generalize its validity and better deal with uncertainty.

For this paper, the HAPESS simulations have been limited at the optical wavelength 532 nm. The correlation between the ash concentration C_a and the zenith-pointing visible Lidar observables β_{hh}, α_{hh}, δ_{co}, and δ_{cr} is shown in Figs. 1 and 2 for each size class VA, FA, CA, SL, and LL and all orientations (PO, OO, TO.2 hereinafter called TO, and also SP, where SP stands for spherical particle). From Figs. 1 and 2, we can observe the following.

1) The plot of ash class centroids in terms of α_{hh} and α_{hh} clearly shows that LL (the largest size class) exhibits the smallest extinction and backscatter, whereas VA

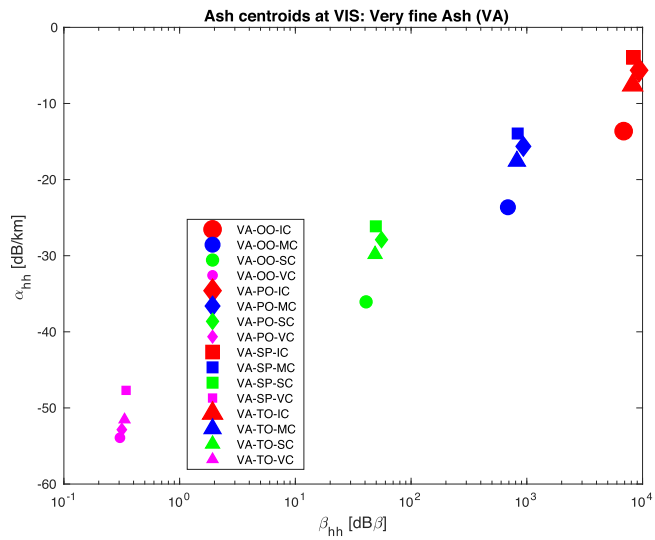

Fig. 1. Correlation between backscattering (in dBβ) and extinction coefficient (in dB/km) for the VA size class in terms of ash concentration and orientation class centroid noting that as the concentration increases, there is an increase of the simulated backscattering and extinction coefficients.

(the smallest size class) exhibits the largest. This is related to the scattering properties at 532-nm wavelength LL scatter in deep optical regime, whereas VA follows the Mie scattering resonances.

2) The LidarLR is almost constant with respect to co-polar backscatter coefficient β_{hh} for all subclasses, but is sensitive to particle orientation. The LidarLR is more dispersed for prolate and oblate orientations depending on the particle size. These variations are due to microphysical differences of the classes and the predominance of the Mie resonant scattering when the particle size is comparable with the wavelength.
3) The co-polar extinction coefficient α_{hh} is also linearly correlated with C_a for all subclasses and for each frequency. The extinction coefficient highlights a similar behavior of the backscatter coefficient.
4) The co-polarization ratio δ_{co} is not significantly correlated with C_a, but is sensitive to the particle orientation and to the frequency, particularly for the size class VA. Indeed, increasing the size class, we can observe that the SP shows a behavior intercepting other orientation (FA, CA, and SL) and mixing for the size class LL.
5) The cross-polarization ratio δ_{cr} is independent of the concentration for all subclasses and varies with TO, PO, OO, and SP orientation models and for each frequency, but this behavior is not clear for the VA size class at each considered frequency.
6) The ash mass concentration C_a is almost linearly correlated with co-polar backscatter coefficient β_{hh} for all subclasses and for each frequency. β_{hh} values of LL are larger than those of the VA class since, for a given concentration, in the wavelength-insensitive optical regime, the Lidar logarithmic response is proportional to the particle concentration number. The latter is smaller for LL particles than do for VA particles since, for a given concentration, the volumetric number of big particles is less than that of small particles.

For inversion purposes, it is worth stressing that ash mass concentration and mean equivalent diameter can be derived from a combination of β_{hh} and α_{hh}, whereas δ_{cr} and δ_{co} may be successfully used to better discriminate the ash classes.

B. Retrieval Algorithm and Parametric Models

Several caveats need to be accepted to properly deal with Lidar products. The major critical issue is the estimation of the range profile of the extinction coefficient α_{xx}, which can be derived by properly inverting the backscatter profiles in the cloud region where the signal is not totally attenuated and using *ad hoc* path attenuation correction algorithms [7], [14]. The latter typically exploits the knowledge of the LR needed to invert the Lidar equation after distinguishing the ash from different aerosol contributions [8], [14], [15]. In order to distinguish spherical from non-SPs, it is crucial to use a polarimetric Lidar instrument [26], [27], [43]. Lidar retrievals are most often based on a solution of the classic Lidar equation, which is a single-scattering approximation that ignores higher order MS. The latter can alter the apparent extinction or transmittance of the medium, produce depolarization of the return signal, and cause a stretching of the return pulse. For most Lidar systems, the magnitude of the multiply-scattered signal is so small these effects are insignificant and can often be ignored without introducing significant errors, but its impact should be considered in some way [43].

The VALR algorithm allows deriving the main ash particles features from polarimetric Lidar observables by means of model-based supervised retrieval algorithm. The algorithm consists of two main steps: ash classification and estimation, both performed in a probabilistic framework using the ML approach. The detection of the ash class from a Lidar polarimetric observable set for each range volume can be performed using an ML identification technique. This technique may be considered a special case of the Bayesian approach. Within the latter, the maximum *a posteriori* probability (MAP) criterion can be used to carry out ash cloud classification in a model-based supervised context [19]. The basic rule is to minimize a proper "distance" (or metric) between the measured and simulated polarimetric set, the latter computed by using the microphysical scattering of each ash class, taking into account both the system noise and the *a priori* available information. If the latter is assumed uniform, MAP becomes the ML method.

The ML technique basically reduces to a minimization process in order to assign the "cth" class to each available Lidar measurement. Under the assumption of: 1) Gaussian-likelihood statistics of the difference between simulated and measured observables and 2) uncorrelation between the differences (errors) of the same observables, the ML method reduces to the minimization of a quadratic form. The estimated ash class c and the retrieved microphysical parameters are those that exhibit the minimum ML square distance d^2 between the Lidar measurement set $\mathbf{x}_m$ and simulated set $\mathbf{x}_s$ of a given class c [16]. If only measurements of attenuation-corrected backscatter coefficient β_{xxmc} and linear cross-polar ratio δ_{crm} are available to define $\mathbf{x}_m$, we can write the following

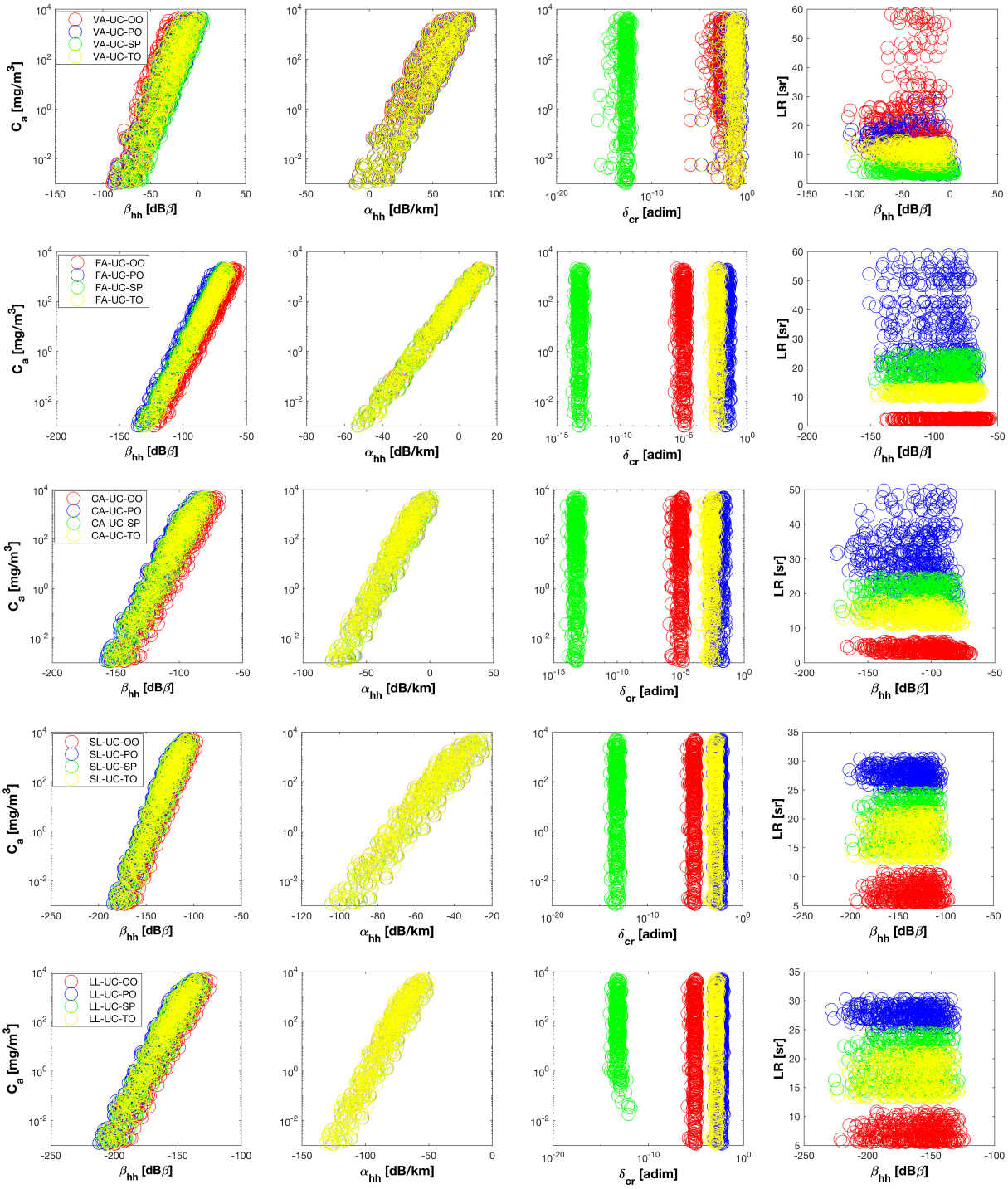

Fig. 2. Numerical results of the HAPESS simulations at 532-nm wavelength (visible). Correlation between ash mass concentration C_a (mg/m^3) and both backscatter (in dBβ) and extinction coefficients (in dB/km) in the top panels (left and right panels, respectively) and between LidarLR and backscatter and between ash mass concentration C_a (mg/m^3) and cross-polarization in the bottom panels (left and right panels, respectively), for each ash class VA, FA, CA, SL, and LL (2×2 panels), for different orientations (OO, PO, SP, and TO) and for uniform concentration (UC) (between 1 and 10^7 μg/m^3). See text and Table I for details.

simplified metrics:

$$\begin{aligned} & d^2\left(C_a^{(c)}, D_n^{(c)}\right) \\ &= \left[\mathbf{x}_m - \mathbf{x}_s^{(c)}\left(C_a^{(c)}, D_n^{(c)}\right)\right]^T \mathbf{C}_{\varepsilon_x \varepsilon_x}^{-1} \left[\mathbf{x}_m - \mathbf{x}_s^{(c)}\left(C_a^{(c)}, D_n^{(c)}\right)\right] \\ &= \frac{\left[\beta_{\mathrm{xxmc}} - \beta_{\mathrm{xxs}}\left(C_a^{(c)}, D_n^{(c)}\right)\right]^2}{\sigma_{\varepsilon_\beta}^{2(c)}} + \frac{\left[\delta_{\mathrm{crm}} - \delta_{\mathrm{xxs}}\left(C_a^{(c)}, D_n^{(c)}\right)\right]^2}{\sigma_{\varepsilon_\delta}^{2(c)}} \end{aligned} \tag{11}$$

where "T" stands for the transpose operator and $\mathbf{C}_{\varepsilon x \varepsilon x}$ is the auto-covariance of the error vector $\varepsilon_x = \mathbf{x}_m - x_s$ with "-1" its inverse. In the simplified ML approach with uncorrelated errors, the terms of (11) are basically weighted by the inverse of variances $\sigma_{\varepsilon\beta}^{2(c)}$ and $\sigma_{\varepsilon\delta}^{2(c)}$ of the simulated data set for the class c. In (11), it is explicit that the simulated vector $\mathbf{x}_s$ depends on the unknown C_a and D_n for each class c.

To retrieve the ash parameters such as concentration and mean size within the selected class c, we can extract their value from the geophysical parameters whose associated $\mathbf{x}_s$ minimizes the quadratic distance (11), that is,

$$\hat{C}_a^{(c)} = C_a^{(c)} | \text{argmin}_{\left(C_a^{(c)}, r_n^{(c)}\right)} \left\{ d^2\left(C_a^{(c)}, D_n^{(c)}\right) \right\} \quad (12a)$$

$$\hat{D}_n^{(c)} = D_n^{(c)} | \text{argmin}_{\left(C_a^{(c)}, r_n^{(c)}\right)} \left\{ d^2\left(C_a^{(c)}, D_n^{(c)}\right) \right\} \quad (12b)$$

where argmin is the function providing the minimum of its argument. It is worth highlighting that these retrievals are conditioned by the numerical forward model accuracy or, in other words, by microphysical–electromagnetic assumptions and their representativeness with respect to the observed scene.

The uncertainty of the ash microphysical estimates in (12), due to noise and the variability of all other geophysical parameters (see Table I), can be derived by taking into account the error statistics around the Lidar-based retrieval distance minimum. By assuming an uncertainty of error vector $\varepsilon_x = \mathbf{x}_m - \mathbf{x}_s$ due to instrumental noise and forward model representativeness, we can define an error threshold δ_ε associated with this uncertainty (e.g., this threshold δ_ε on the backscatter coefficient can be assumed between 10% and 50%, here typically assumed to be 20%). Thus, standard deviations σ_{Ca} and σ_{Dn} of ash concentration and mean diameter estimates, respectively, are given by

$$\sigma_{\hat{C}_a}^{(c)} = \text{std}\left\{ C_a^{(c)} | d^2\left(C_a^{(c)}, D_n^{(c)}\right) < \delta_\varepsilon^2 \right\} \quad (13a)$$

$$\sigma_{\hat{D}_n}^{(c)} = \text{std}\left\{ D_n^{(c)} | d^2\left(C_a^{(c)}, D_n^{(c)}\right) < \delta_\varepsilon^2 \right\} \quad (13b)$$

where std is the standard deviation function.

In the literature, we can find several parametric models allowing deriving the ash concentration from the measured backscatter coefficient. The appealing feature of parametric retrieval techniques is their simplicity in the application to measurements sets, even though the downside is less flexibility (due to the fixed regression model) and frequency scalability (due to the prescribed coefficients valid at a given wavelength).

The first retrieval parametric model (hereinafter PM1), employed to evaluate the ash concentration C_{aPM1} [g/m^3] from ash backscattering, is based on the following relation [27]:

$$C_{\text{aPM1}} = k_c \langle R_{\beta\alpha x} \rangle \rho_a \beta_{\text{xxmc}} \quad (14)$$

where k_c is the ash conversion factor, function of the PSD. For a large masse, k_c is mainly dependent on the ash effective radius r_{ep} [see (1)] and given by $(2/3) \cdot r_{\text{ep}}$ [10], [29], [33]. In [22], a value of about 10 μm is assumed for r_{ep} so that k_c is hence set to 0.6×10^{-5} m. In (13), $\langle R_{\beta\alpha x} \rangle$ is the mean value of the estimated LidarLR [1], [2], [22], ρ_a is the density of volcanic ash fixed to 2450 kg/m^3 [31], and β_{hhm} is the measured volcanic ash backscatter coefficient [39]. The errors on ash mass concentration are evaluated from the uncertainties of $R_{\beta\alpha x}$, β_{hhm}, and ρ_a and reach a value of 55%. An additional uncertainty of about 50% must be considered due to the assumption of the effective radius [22], [33]. In the absence of other sources, we can derive D_{np} from VALR-ML and assume $r_{\text{ep}} = D_{\text{np}}/2$ to estimate k_c in (13).

Another parametric approach, hereinafter referred to PM2, to derive the ash concentration C_{aPM2} [g/m^3] from the measured ash backscatter [13], [10] can be expressed as

$$C_{\text{aPM2}} = \lfloor 1.346\ r_{\text{ep}} - 0.156 \rfloor \langle R_{\beta\alpha x} \rangle \beta_{\text{xxmc}} \quad (15)$$

where r_{ep} is the ash effective radius. The expression between square brackets is known as the mass–extinction conversion factor for volcanic ash concentration, depending on the particle effective radius r_{ep} [10], [13]. Indeed, if the information about the effective radius is not available, we can use a simplified version of (14), where the square brackets can be substituted by the mass–extinction conversion factor of 1.45 g/m^2 (95% of the compatible ensembles are in the range 0.87–2.32 g/m^2) [10]. The relative uncertainty of the retrieved mass concentration is estimated to be about 40% and mainly caused by the uncertainty of the microphysics of the particles (size distribution, refractive index, and shape) [13]. As in (13), if not available elsewhere, we can derive $r_{\text{ep}} = D_{\text{np}}/2$ from VALR-ML.

Both parametric PM1 and PM2 models have some *a priori* information derived from the literature or available sources and exploit the correlation between concentration and backscatter. Indeed, by exploiting the HAPESS forward model illustrated in Section II-A, we can derive a parametric regressive formula, hereinafter named VALR-Reg, valid at visible wavelengths. A logarithmic relation for estimating ash concentration $C_{\text{aVALR}_{\text{Reg}}}$ [g/m^3] can be expressed as follows:

$$\hat{C}_{\text{aVALR}_{\text{Reg}}} = 10^{[a_{\text{VA}} + b_{\text{VA}} (\log_{10} \beta_{\text{xxmc}})]} \quad (16)$$

where a_{VA} and b_{VA} (0.8643 and 0.8370) are regressive coefficients, derived from HAPESS simulations, including all particle orientations (OO, PO, SP, and TO) for VA size class (D_n between 0.125 and 8 μm).

C. Multiple Scattering Impact

We can attempt to evaluate the uncertainty in the estimated particle extinction due to MS within clouds or aerosol layers. If the particle effective radius becomes larger, the probability of MS increases since a stronger forward scattering causes photons to remain in the field of view (FOV) of the detector. This MS effect typically leads to an increase of the particle backscatter up to 50% and a consequent underestimation of path attenuation or atmospheric optical depth up to 30% [24]. The MS can affect the Lidar measurements, especially in the presence of large optical thicknesses. The MS signal increases as the laser beam divergence, the FOV of the receiver, and the distance between the laser source and the investigated volume increase [24], [46].

Modeling MS effect in Lidar response is not an easy task due to path dependence and optical thickness variability. In order to test the sensitivity of backscatter coefficient to the MS, we can simulate its impact on the backscatter coefficient by introducing an MS factor f_{MS} within the conventional Lidar equation. This MS factor f_{MS} is by construction defined between 0 (no MS present) and 1 (full MS). The MS-affected

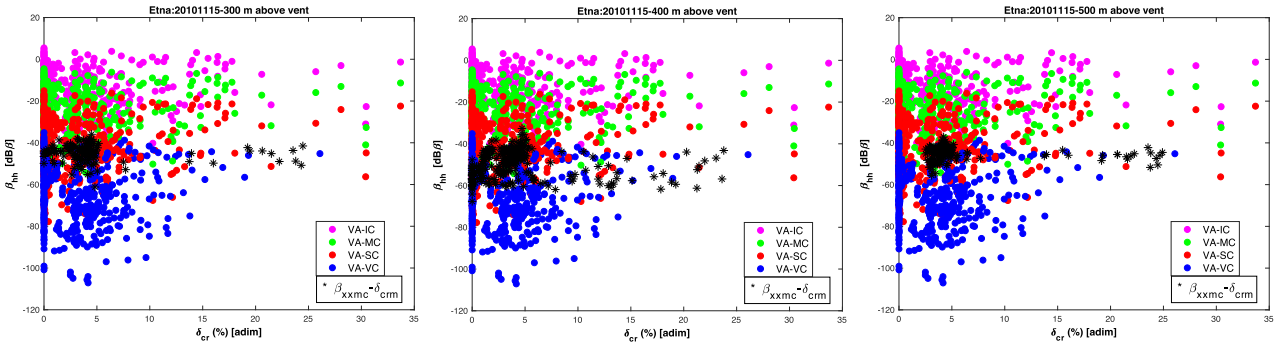

Fig. 3. Lidar data collected during the November 15, 2010 ash emission at Mt. Etna in Italy. Superimposition between measured (dark dots) and simulated backscatter coefficient β_{hh} (in dBβ) and cross-polarization ratio δ_{cr} (in %) at (Left) 300, (Middle) 400, and (Right) 500 m of altitude above Etna summit craters, respectively. Different color identifies different concentration classes (IC in magenta, MC in green, SC in red, and VC in blue), all for the VA class.

measured backscatter coefficient can be expressed as

$$\beta_{\mathrm{xxm}}^{\mathrm{MS}}(s) = \beta_{\mathrm{xxm}}(s)e^{2\tau(s)f_{\mathrm{MS}}} = \beta_{\mathrm{xxmc}}(s)e^{-2}\tau\ (s)e^{2\tau(s)f_{\mathrm{MS}}} = \beta_{\mathrm{xxmc}}(s)e^{-2}\tau(s)(1-f_{\mathrm{MS}}) \tag{17}$$

where s is the range coordinate and τ is the optical thickness (due to the integral of the extinction coefficient α_{xx}) along the two-way path. For simplicity, f_{MS} has been assumed to be range independent, whereas the quantity $\tau(1-f_{\mathrm{MS}})$ can be interpreted as the "apparent" optical thickness affected by MS radiation recovery.

In order to evaluate the uncertainty of the ash concentration and mean diameter estimates due to MS effects, we can perform a sensitivity analysis by replacing the measurements Lidar data set (corrected for two-way path attenuation 2τ) with the corresponding quantity $\beta_{\mathrm{xxmc}}^{\mathrm{MS}}$ in (17) where f_{MS} is supposed to be between 0 and 0.3, whereas τ is taken, as a first approximation, from the path-attenuation correction algorithm. This simplified approach does not aim at quantifying the MS effects, but only the sensitivity of the retrievals to its presence. In this respect, we define the total MS standard deviations of C_a and D_n as

$$\sigma_{C_a\mathrm{MS}} = \sqrt{\sigma_{\hat{C}_a}^2 + \sigma_{\hat{C}_a f\mathrm{MS}}^2} \tag{18a}$$

$$\sigma_{D_n\mathrm{MS}} = \sqrt{\sigma_{\hat{D}_n}^2 + \sigma_{\hat{D}_n f\mathrm{MS}}^2} \tag{18b}$$

where $\sigma_{\hat{C}_a}^2$, $\sigma_{\hat{D}_n}^2$, $\sigma_{\hat{C}_a f_{\mathrm{MS}}}^2$, and $\sigma_{\hat{D}_n f_{\mathrm{MS}}}^2$ are the standard deviations of concentration and mean diameter without and with the MS contribution, respectively.

III. Application to Etna Case Studies

The ML retrieval methodology has been tested on two Etna eruptions: the ash emission of November 15, 2010 and the lava fountain of August 12, 2011. We have applied the VALR-ML to Lidar data in order to retrieve the ash concentration and ash particle mean diameter using (12). These retrievals are also compared with those already estimated in [30] and [33] in order to show the VALR-ML potential.

The VAMP scanning Lidar system, whose measurement results are used in this paper, transmits a linearly polarized laser light at 532-nm wavelength and detects parallel and cross-polarized components of the elastic backscattered simultaneously. The VAMP system allows moving in azimuth and elevation with the possibility to scan the volcanic plume either horizontally and/or vertically at a maximum speed of 0.1 rad/s. This system was installed at the "M.G. Fracastoro" astrophysical observatory (14.97° E, 37.69° N), located at 1760 m on the SW flank of the volcano, only 7 km away from the Etna summit craters, allowing the laser beam to scan the atmosphere around the summit craters.

The attenuation-corrected measured backscatter coefficients β_{xxmc} in (10) have been obtained by using the Klett–Fernald algorithm [8], [15]. The LR, as defined in (7), has been assumed to be about 36 sr inside the plume, as described in [22], whereas the contribution of background aerosol load was considered negligible, less than about 10^7 m$^{-1}\cdot$sr^{-1} in the Mediterranean region in clear-sky conditions [36]. Details on the Lidar data processing can be found in [22].

To train the VALR-ML algorithm, considering the typical Etna eruption modes and the available observations of distal plumes, we have used a simulated data set (see Sections II-A and II-B) consisting of the smallest ash class, VA, with orientation classes TO, OO, PO together with a class SP. The validity of these *a priori* choices can be assessed by comparing the measured and simulated observables for both case studies. Note that in the two analyzed study cases, we have selected only the backscatter coefficients correlated with optical depths less than 0.5 and depolarization between 0.1 and 0.5 of ash plume close to Lidar system (about 6 km) in order to avoid any possible MS influence.

A. Etna Ash Emission in 2010

The first case study is related to ash emission observed by the VAMP system on November 15, 2010 when both backscatter and depolarization channels were available. During this event, ash emissions from the North East Crater and high degassing from the Bocca Nuova Crater were clearly visible [33]. Water vapor and ash emission occurred every 1–2 min, as reported by volcanologists during a field survey at the summit craters. Different volcanic plume sections were obtained by pointing the laser beam with a fixed

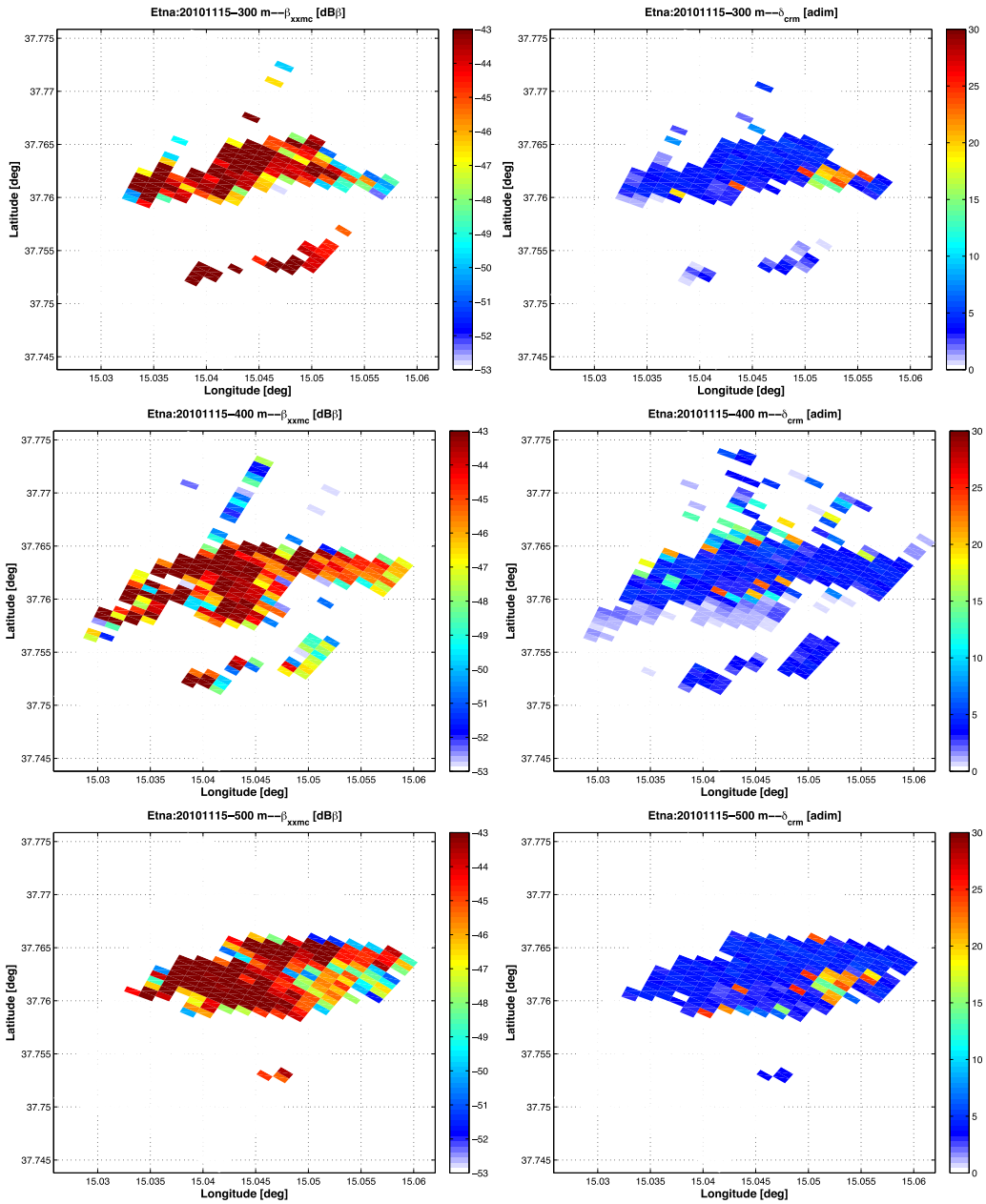

Fig. 4. Lidar data collected during the November 15, 2010 ash emission at Mt. Etna in Italy. Maps of the measured backscatter coefficient (in dBβ) and linear volumetric depolarization (in %), left and right panels, respectively, at each elevation (300, 400, and 500 m) above the Etna summit craters.

direction defined by azimuth angle of 17.3° and three different elevations (14.4°, 14.65°, and 14.9°), corresponding approximately to altitudes of 300, 400, and 500 m above summit craters (we will refer to these elevations in terms of corresponding altitudes in the following text) [33].

As mentioned, in order to find the ash size classes best fitting the measured backscatter at the three elevations, we have first selected a simulated data subset to train the VALR-ML algorithm. Fig. 3 shows both measured and simulated ash backscatter and cross-polarization coefficient, expressed in dBβ and in percent, respectively, for VA size class with IC, MC, SC, and VC concentrations (see Table I).

Measured Lidar observables are fairly well represented and consistent with the simulated ones. In the ash plume layer, β_{xxmc} reaches values larger than 2×10^{-5} m$^{-1} \cdot$ sr^{-1} (-47 dBβ) with the highest values of about 5×10^{-5} m$^{-1} \cdot$ sr^{-1} (-43 dBβ), usually associated with a larger concentration of volcanic aerosols [32]. In all cases, the average and maximum linear cross-polarization is about 4%–6% and 24%–26%, respectively. The latter values are a clear indication of a complex morphology of ash particles, the relatively high cross-polarization being a significant indicator of nonsphericity [42].

It is worth remembering that the uncertainty of δ_{crm} comes primarily from systematic errors in the setup of the Lidar systems, which cannot be reduced by statistical methods. Indeed, we have found that the main error sources originate from the depolarization calibration (with large differences

TABLE II

PERCENTAGE RATIO BETWEEN THE STANDARD DEVIATION ($\sigma_{Ca}/\langle C_a\rangle$ AND $\sigma_{Dn}/\langle D_n\rangle$) AS WELL AS OVERALL MS-INCLUDED STANDARD DEVIATION ($\sigma_{CaMS}/\langle C_a\rangle$ AND $\sigma_{DnMS}/\langle D_n\rangle$) WITH RESPECT TO THE AVERAGE RETRIEVED VALUE FOR BOTH CONCENTRATION AND MEAN DIAMETER, RESPECTIVELY, CONSIDERING VARIOUS f_{MS} (0, 0.1, 0.2, AND 0.3) FOR THREE CASES: 1) AT THREE ELEVATIONS DURING THE NOVEMBER 15, 2010 ERUPTION (USING THE DEPOLARIZATION MEASUREMENTS); 2) DURING THE ETNA ERUPTION ON AUGUST 12, 2011 (USING THE DEPOLARIZATION MEASUREMENTS); AND 3) PROFILE OF ASH PLUME ON AUGUST 12, 2011 (USING THE FULL DATA SET)

	Altitude [m]	Uncertainty [%]	f_{MS} = 0	f_{MS} = 0.1	f_{MS} = 0.2	f_{MS} = 0.3
a)	300	$\sigma_{Ca}/\langle C_a\rangle$	39.44	-	-	-
		$\sigma_{CaMS}/\langle C_a\rangle$	-	42.70	41.98	41.04
		$\sigma_{Dn}/\langle D_n\rangle$	3.83	-	-	-
		$\sigma_{DnMS}/\langle D_n\rangle$	-	5.65	5.98	5.96
	400	$\sigma_{Ca}/\langle C_a\rangle$	82.75	-	-	-
		$\sigma_{CaMS}/\langle C_a\rangle$	-	89.28	88.23	84.30
		$\sigma_{Dn}/\langle D_n\rangle$	9.88	-	-	-
		$\sigma_{DnMS}/\langle D_n\rangle$	-	14.23	14.78	14.93
	500	$\sigma_{Ca}/\langle C_a\rangle$	41.14	-	-	-
		$\sigma_{CaMS}/\langle C_a\rangle$	-	45.25	44.62	42.95
		$\sigma_{Dn}/\langle D_n\rangle$	4.17	-	-	-
		$\sigma_{DnMS}/\langle D_n\rangle$	-	6.22	6.47	6.39
	Elevation [deg]	Uncertainty [%]	f_{MS} = 0	f_{MS} = 0.1	f_{MS} = 0.2	f_{MS} = 0.3
b)	20-59	$\sigma_{Ca}/\langle C_a\rangle$	4.41	-	-	-
		$\sigma_{CaMS}/\langle C_a\rangle$	-	6.13	5.87	5.57
		$\sigma_{Dn}/\langle D_n\rangle$	8.33	-	-	-
		$\sigma_{DnMS}/\langle D_n\rangle$	-	12.77	12.21	11.81
	Elevation [deg]	Uncertainty [%]	f_{MS} = 0	f_{MS} = 0.1	f_{MS} = 0.2	f_{MS} = 0.3
c)	Profile	$\sigma_{Ca}/\langle C_a\rangle$	1.22	-	-	-
		$\sigma_{CaMS}/\langle C_a\rangle$	-	1.22	1.22	1.22
		$\sigma_{Dn}/\langle D_n\rangle$	4.68	-	-	-
		$\sigma_{DnMS}/\langle D_n\rangle$	-	7.55	6.78	7.10

between different calibration methods) and by backscatter coefficient correction due to the uncertainty in the height-dependent LidarLR and the uncertainty in the signal calibration in the assumed clean and free troposphere [9]. High particle depolarization values of about 30%–35% are observed in the main volcanic ash layer and are similar to those found elsewhere with values of 35%–38% [2], [5], [24]. The latter values suggest a large fraction of volcanic aerosols. Low values of δ_{crm} and values between $1\% < \delta_{\mathrm{crm}} < 2\%$ are typically associated with SPs [13].

Fig. 4 shows, for each considered elevation (labeled with respect to height in meters above the crater), the measured backscatter coefficient, again expressed as dBβ, and the volumetric depolarization ratio. The latter presents a variability between 2% and 25%, whereas few pixels show higher values. By applying the VALR-ML algorithm to data of Fig. 4, Fig. 5 shows the ash concentration and mean diameter retrievals, considering both measured Lidar observables β_{xxmc} and δ_{crm} and only the backscatter coefficient β_{xxmc}. The latter indicates that at each elevation angle and when we consider both the measured Lidar observables, the average concentration is about 8.63 ± 6.04 mg/m^3 and the mean diameter is about 3.37 ± 2.04 μm. If only the backscatter coefficient is taken into account, the average concentration is about 13.01 ± 4.50 mg/m^3 and the mean diameter about 5.80 ± 2.46 μm. This means that using only backscatter measurements, the retrieved values are on average larger than about 66% and 58% for concentration and mean diameter, respectively, with respect to the two-observable setup. A more complete set of Lidar observables (two or more) tends to preserve the smaller sizes and concentrations with a larger variability (standard deviation) of both ash concentration and mean diameter. Note also that VALR-ML retrieval results suggest that the availability of depolarization measurements: 1) provides a more likely retrieval of non-SPs with a given shape/orientation and 2) has a positive impact on the class discrimination.

Standard deviations $\sigma_{\hat{C}_a}$ and $\sigma_{\hat{D}_n}$ of the Lidar-based VALR-ML retrievals can be estimated using (13) for both ash concentration and mean diameter, respectively. As mentioned in Section II-C, the impact of MS can be at least evaluated in terms of increased uncertainties $\sigma_{\hat{C}_a f_{\mathrm{MS}}}$ and $\sigma_{\hat{D}_n f_{\mathrm{MS}}}$ of the Lidar-based retrievals, playing with the MS factor f_{MS} defined in (17). In this respect, block a) of Table II shows the uncertainties as percentage ratio of the averaged standard deviation $\langle\sigma_{\hat{C}_a}\rangle$ (without MS effects) and $\langle\sigma_{\hat{C}_a f_{\mathrm{MS}}}\rangle$ (with MS effects) with respect to the average $\langle\hat{C}_a\rangle$ as well as the percentage ratio for the estimate of the mean diameter $\hat{D}_n$. Note that the average values are computed over all the performed retrievals and are needed to introduce an overall score. The results of Table II indicate that on average both ash concentration and mean diameter retrievals are not very sensitive to MS effects (e.g., concentration estimate uncertainty goes from about 40% up to 43%, whereas the mean diameter one from 4% up to 7%). Indeed, mean diameter estimates seem to be more affected by the increase of the MS fraction f_{MS}. This is not surprising since, as already mentioned, we have properly selected only measurements close to the Lidar system (about 6 km) in order to limit any possible MS influence.

B. Etna Lava Fountain in 2011

The second test case analyzed here is related to the Etna lava fountain of August 12, 2011, when both backscatter

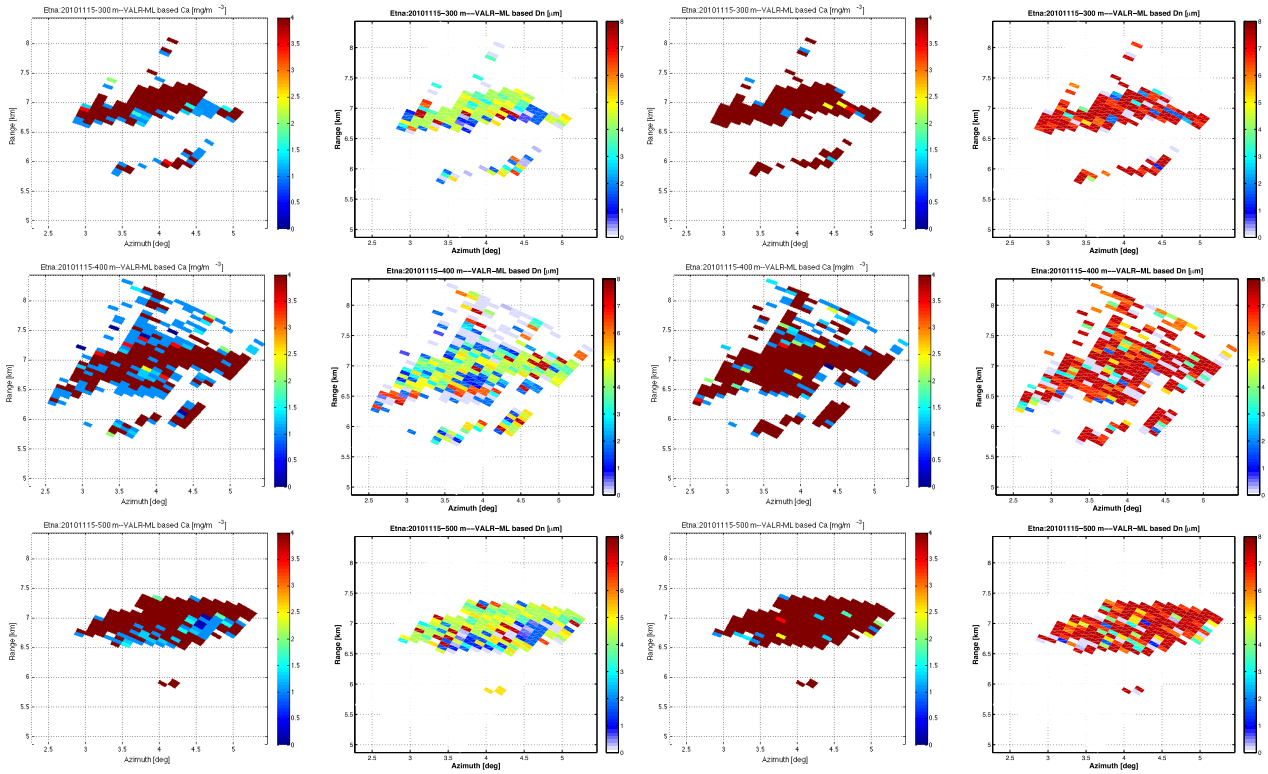

Fig. 5. Mt. Etna eruption on November 15, 2010. Maps of VALR-ML estimates of ash concentration and mean diameter at each elevation at 300, 400, and 500 m (first, second, and third rows, respectively) above the summit crater of Mt. Etna using: 1) both measured Lidar observables (first two columns on the left) β_{xxmc} and δ_{crm} and 2) only the backscatter coefficient (last two columns on the right) β_{xxmc}.

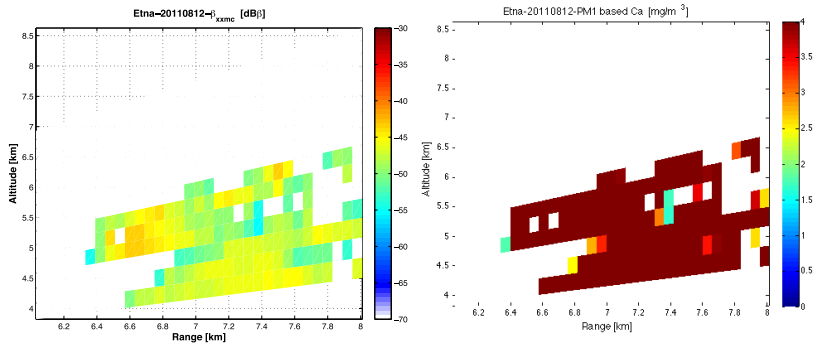

Fig. 6. Lidar data collected during the August 12, 2011 lava fountain event at Mt. Etna in Italy. (Left) Cross section of the measured backscatter coefficient (in dBβ) of ash plume as a function of altitude above the craters and range. (Right) PM1 retrieval of ash concentration considering a $r_{\mathrm{eff}} = 10\ \mu$m.

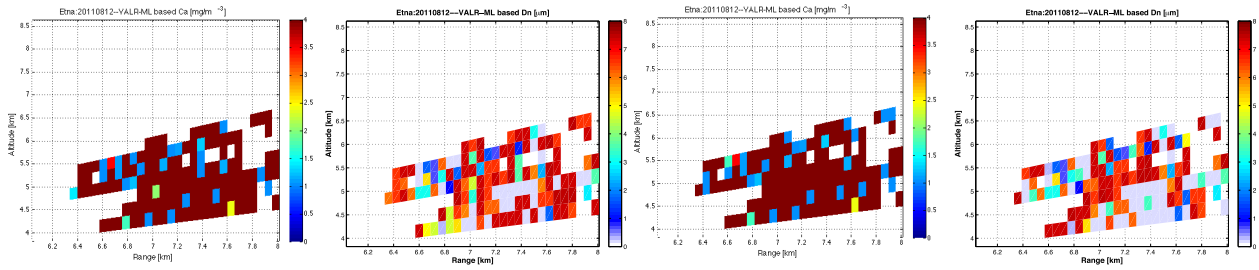

Fig. 7. Lidar data collected during the lava fountain event on August 12, 2011 at Mt. Etna Italy. Cross sections of VALR-ML estimates of ash concentration and mean diameter, respectively, considering a (left two panels) complete HAPESS simulation data set and (right two panels) partial simulation data set without spherical particles.

and depolarization channels were available. The scanning by the VAMP system was performed by changing the elevation angle between 20° and 59° with a fixed azimuth of 36.7°. Lidar measurements were acquired from 08:59 till 11:56 UTC. The volcanic particles were observed between 6.5 and 8 km from the Lidar station along the laser beam path, when

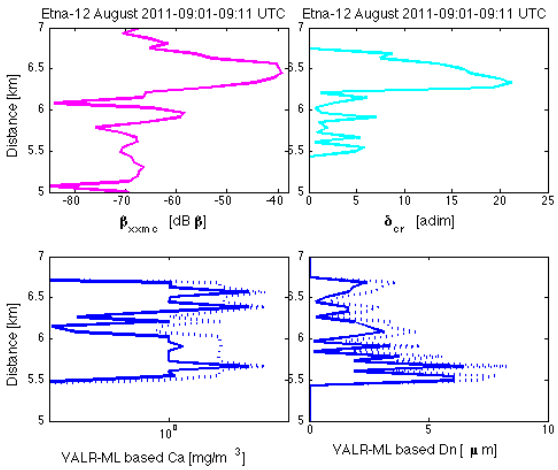

Fig. 8. Lidar data collected at 09:01–09:11 UTC during the August 12, 2011 lava fountain event at Mt. Etna in Italy. (Top panels) Range profiles of ash backscattering and depolarization measured by the VAMP system at Serra La Nave station. (Bottom panels) VALR-ML estimated ash concentration and mean diameter(solid curve) together with the same estimates plus its standard deviation (dashed curve) derived from (12).

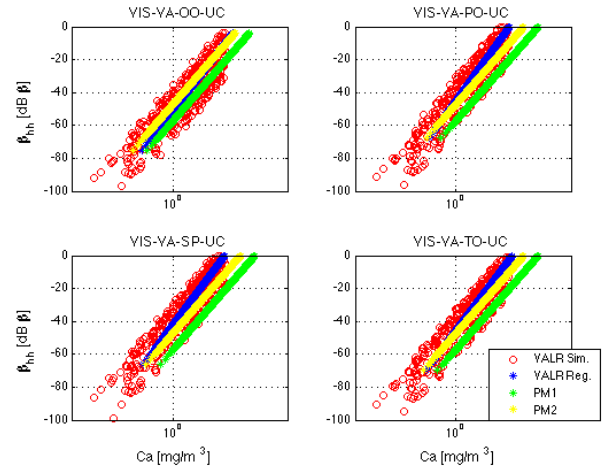

Fig. 9. Correlation between the backscatter coefficient (in dBβ) and the ash concentration (in g/m^3) derived from: 1) the HAPESS simulations (red dots) referring to VA class with OO, PO, SP, and TO orientation (see title of each panel) and 2) parametric models VALR-Reg (blue dots), PM1 (yellow dots), and PM2 (green dots), respectively.

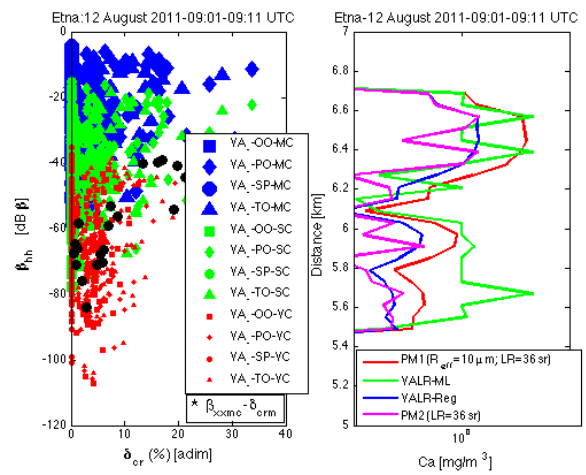

Fig. 10. Etna eruption on August 12, 2011 at 09:01–09:11 UTC. (Left) Comparison between the simulated (colored dots for each considered class in Table I) and measured backscatter coefficient (black dots, in dBβ) and cross-polarization ratio (black dots, in %). (Right) Profile of the concentration estimates derived from PM1 (with effective radius equal to 10 μm), PM2, VALR-Reg, and VALR-ML algorithms.

a column height of about 7 km above sea level was present, as shown by the cross section of the corrected backscatter coefficient in Fig. 6 [30].

We have used the same simulated training data set, previously discussed in Section II-A, obtaining the most likely ash size classes similar to those on November 15, 2010 but with a larger ash concentration (about one order of magnitude), as shown in Fig. 6 (right). The latter is derived from the PM1 algorithm showing a mean concentration of about 9 mg/m^3.

The VALR-ML-derived ash concentration and mean diameter are shown in Fig. 7, considering a training data set with (complete) and without (partial) SPs. In both cases, the average concentration is about 65.00 $\pm$ 37.3 mg/m^3 and the mean diameter is about 3.01 $\pm$ 1.2 μm as shown in Table III, which also includes the sensitivity analysis due to the inclusion or exclusion of spherical particles within the training data set. The percentage ratio between the number of spherical classes and the number of total detected ash classes is about 37%. This ratio underlines the impact of volumetric depolarization measurements useful to distinguish the ash particle category. It is remarkable how the lack of depolarization observables does not significantly affect the retrievals of ash size and concentration.

Note that for this case study, an independent estimate, based on ground measurements and forecast model simulations, of the ash PSD is available in terms of percentage weight [30]. The latter is obtained using the Lagrangian numerical PUFF model [34], [38] inside the region investigated by Lidar [30]. The measured size distribution is clearly asymmetric, well approximated by a log-normal or a Gamma distribution [30]. The PUFF-based average ash particle size is about 5.3 μm, slightly larger than VALR-ML-based mean diameter retrieval (3.01 $\pm$ 1.22 μm).

Fig. 8 shows the range profiles of the measured backscattering coefficient and depolarization ratio, obtained by pointing the VAMP laser beam toward the plume for 10 min (09:01–09:11 UTC) and when the eruption column reached the height of 9 $\pm$ 0.5 km. Lidar profiles show two layers with different properties. The first ash layer, at 6.1 km from the Lidar station along the laser beam, is characterized by lower β_{xxmc} of about -58 dBβ and δ_{crm} of about 5%. The second ash layer, located between 6.2 and 6.8 km, is characterized by high peak values of β_{xxmc} of about -41 dBβ and δ_{crm} of about 20%, suggesting that volcanic ash was mainly contained in this layer [30].

The VALR-ML retrievals in terms of concentration and mean diameter are also shown in the lower panels of Fig. 8. The ash concentration peak is about 100 mg/m^3, whereas the mean diameter reaches a maximum value of 6.3 μm. In order to attribute an uncertainty to VALR estimations, we have assumed a backscattering coefficient error of 50% so that

TABLE III

MEAN VALUE (MEAN) AND STANDARD DEVIATION (STD) OF THE VALR-ML ESTIMATES OF VA CONCENTRATION AND MEAN DIAMETER DURING THE ETNA LAVA FOUNTAIN ON AUGUST 12, 2011 CONSIDERING THE HAPESS SIMULATED DATA SET WITH BOTH SPHEROIDAL AND SPHERICAL PARTICLES (COMPLETE) AND WITHOUT SPS (PARTIAL)

	DataSet (VA)	Elevation range [°]	Concentration [mg/m^3]	Mean diameter [μm]	Detected ash classes and occurrence
LIDAR estimates using VALR-ML	OO, PO, TO, MC, SC, VC	20-59	Mean: 67.46 Std: 37.84	Mean: 2.89 Std: 1.18	VA-OO: 31 VA-PO: 79 VA-TO: 31
	OO, PO, TO, MC, SC, VC + SP	20-59	Mean: 62.52 Std: 36.84	Mean: 3.13 Std: 1.27	VA-OO: 21 VA-PO: 49 VA-SP: 52 VA-TO: 19

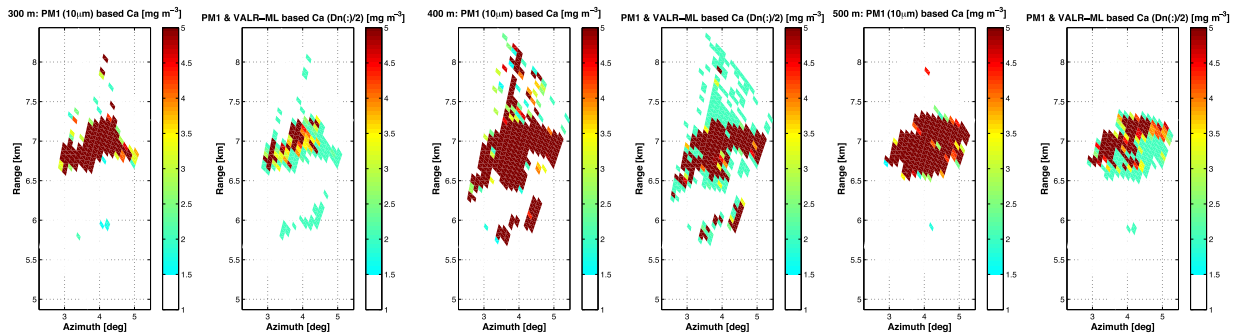

Fig. 11. Etna eruption on November 15, 2010. Panels (first, second, and third couple of plots) are related to elevations at 300, 400, and 500 m above the Etna summit craters. Ash concentration derived by the PM1 retrieval using: 1) (left panel of each couple of plots) an ash effective radius of 10 μm as in [33] and 2) (right panel of each photograph) the mean radius derived from the VALR-ML retrieval for each detected pixel, as shown in Fig. 5.

the standard deviation of both ash concentration and mean diameter are evaluated and associated with each estimate, as in (12). This uncertainty is shown in Fig. 8. Note that there are ranges in Fig. 8 where, for a higher backscatter, we can retrieve a lower concentration from VALR-ML. This may seem a contradiction, but looking at (3), we realize that the same β_{xxmc} can be associated with a large concentration of small particles or, vice versa, with a small concentration of large particles. Thus, the simultaneous retrieval of both C_a and D_n is essential to interpret this ambiguity.

The impact of MS in this case study shows the same behavior of the previously analyzed case, as shown in blocks *b*) and *c*) of Table II. Indeed, the uncertainty, expressed as a percentage ratio, highlights how a smaller variability of ash concentration and mean diameter is associated with an increase of f_{MS}, especially for higher altitudes.

C. Comparison With Parametric Model Retrievals

There is a reasonable interest in comparing the VALR-ML technique with other parametric methods in order to understand the potential of a physically based approach with respect to more straightforward parametric procedures.

The HAPESS forward model simulations at 532 nm can provide an effective way to compare the three parametric retrieval approaches (13)–(15) together with VALR-ML. Fig. 9 shows the HAPESS simulations superimposed on results of the selected models PM1 in (13) (assuming LR = 36 sr and $r_{\mathrm{eff}} = \langle D_n \rangle/2$ from the considered size class) and PM2 in (14) (assuming a default mass–extinction conversion factor of 1.45 g/m^2 and $r_{\mathrm{eff}} = \langle D_n \rangle/2$ from the considered size class) together with VALR-Reg in (15). The PM1 formula for all orientations shows a higher ash concentration, whereas the PM2 typically lies between PM1 and VALR-Reg (which is the best approximation of HAPESS simulated data by definition). For the same backscatter coefficient, the VALR-Reg model tends to predict a larger ash concentration. Indeed, VALR-ML estimates may be larger or smaller than VALR-Reg as the forward model simulations are randomly distributed around the regression curve. This is due to the inherent best-fitting approach of the VALR-Reg model (and any other regressive approach) that is based on a minimization of the simulated points with respect to the modeled regression curve.

A first example of intercomparison is shown in Fig. 10 where the profile of Fig. 8, related to August 12, 2011 Lidar data, is reconsidered. In the left panel, the HAPESS simulations and the few measured samples are superimposed. The right panel highlights the estimates of three analyzed parametric models compared with the VALR-ML one, already shown in Fig. 8. The PM1 parameters in (13) are similar to those in Fig. 9, but $r_{\mathrm{eff}} = 10$ μm as assumed in [30], whereas PM2 is applied without modifications. PM1 estimates, in this setup, are not always larger than the others, whereas VALR-ML ones are typically but not necessarily lower, being PM2 and VALR-Reg in the bottom.

A second application of the parametric retrieval models is shown in Fig. 11 for the event of Etna eruption on November 15, 2010. Fig. 11 is, indeed, the output of a sensitivity study as it plots both retrievals from PM1 in (13) using $r_{\mathrm{eff}} = D_n/2$ derived from VALR-ML and PM1 with a fixed value $r_{\mathrm{eff}} = 10$ μm as assumed in [30]. As expected, VALR-ML-based ash concentration retrievals are partly lower than those of PM1 due to the difference in the average particle size. This points out the impact of an arbitrary assumption of the effective ash radius on ash retrievals.

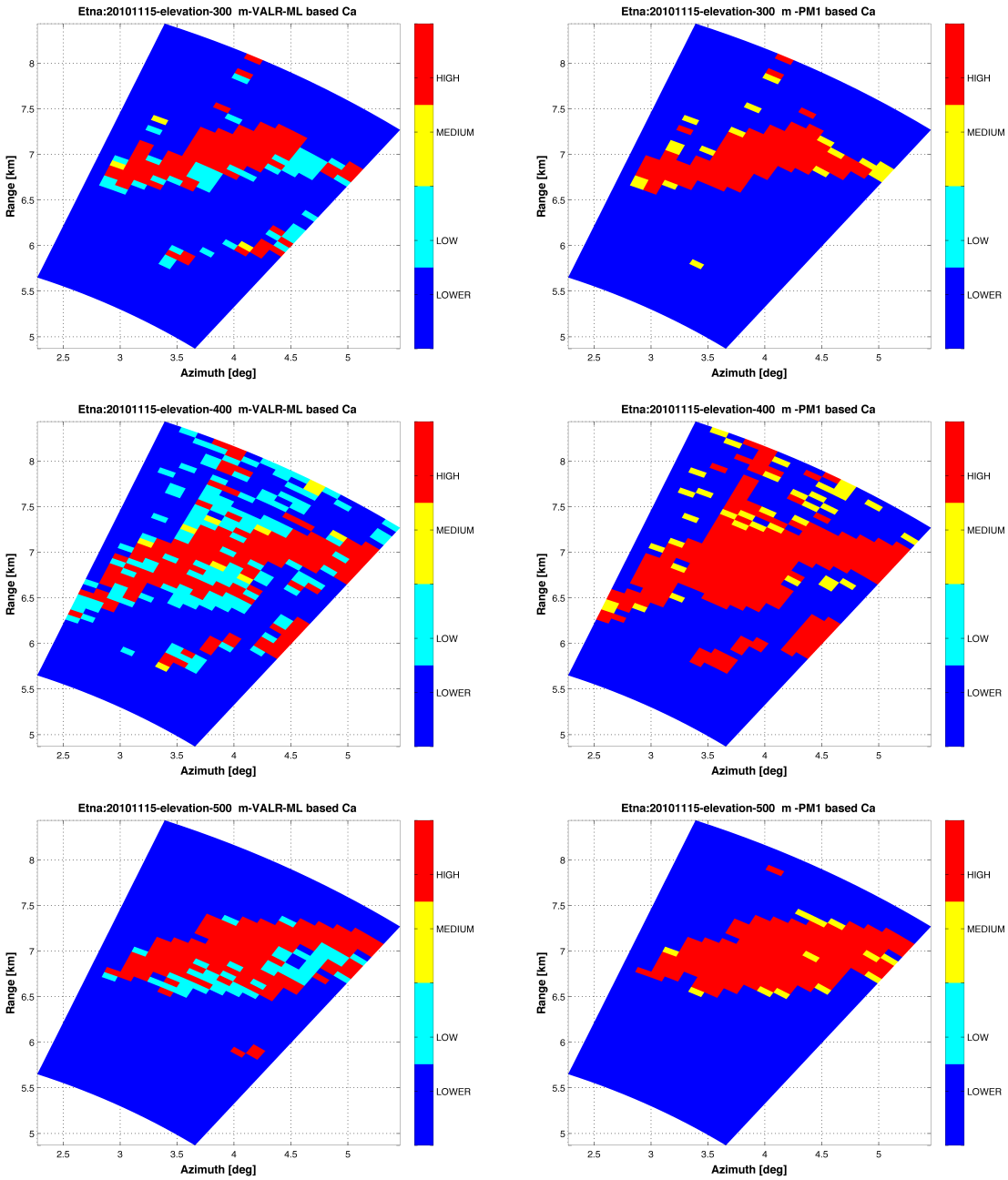

Fig. 12. Etna eruption on November 15, 2010. Ash concentration range maps obtained applying the (Left) VALR-ML-derived mass concentration and (Right) PM1-derived mass concentration and referred to 300, 400, and 500 m of elevation. Different colors identify the area of LOWER ($<2 \times 10^{-4}$ g/m^3), LOW (2×10^{-4} g/m^3 – 2×10^{-3} g/m^3), MEDIUM (2×10^{-3} g/m^3 – 4×10^{-3} g/m^3), and HIGH ($>4 \times 10^{-3}$ g/m^3) ash contamination defined by the ICAO regulations.

The Lidar data analysis may help quantifying the impact that ash emissions may have on aviation safety in order to prevent flights in areas of high ash contamination whose lower threshold is 2×10^{-4} g/m^3 in compliance with the International Civil Aviation Organization (ICAO) directives. In this respect, besides 2×10^{-4} g/m^3, we can define four concentration ranges using increasing ash concentration values equal to 2×10^{-3}, 3×10^{-3}, and 4×10^{-3} g/m^3. Using these thresholds, we can identify four areas: LOWER (less than 2×10^{-4} g/m^3), LOW (between 2×10^{-4} and 2×10^{-3} g/m^3), MEDIUM (between 2×10^{-3} and 4×10^{-3} g/m^3), and HIGH (larger than 4×10^{-3} g/m^3).

The results are shown in Fig. 12 in terms of spatial maps for the November 15, 2010 Etna eruption. These panels refer to elevations corresponding to altitudes of 300, 400, and 500 m, respectively, (see Fig. 4) and shows only the ash concentration maps retrieved from VALR-ML and PM1 (setup as in Fig. 11 which as a standard configuration [30]). As expected, for each elevation, VALR-ML ash concentration retrievals are generally lower than those derived from PM1.

TABLE IV

CONTINGENCY TABLE RELATED TO ASH CONCENTRATION MAP AT THREE ELEVATIONS DURING THE NOVEMBER 15, 2010 ETNA ASH EMISSION, RELATED TO THREE DIFFERENT CONCENTRATION THRESHOLDS (SEE TEXT FOR DETAILS)

		PARAMETRIC RETRIEVAL MODEL (PM1)					
	H	$Th_1=2*10^{-4}$ [g/m^3]		$Th_2=2*10^{-3}$ [g/m^3]		$Th_3=4*10^{-3}$ [g/m^3]	
VALR-ML ALGORITHM	300	HIT: 97.38%	MISS: 0%	HIT: 54.90%	MISS: 11.11%	HIT: 47.71%	MISS: 16.33%
		FALSE: 2.62%	NEG: 0%	FALSE: 21.56%	NEG: 12.41%	FALSE: 15.68%	NEG: 20.26%
	400	HIT: 96.92%	MISS: 0%	HIT: 52.30%	MISS: 2.46%	HIT: 49.23%	MISS: 2.47%
		FALSE: 3.08%	NEG: 0%	FALSE: 36.30%	NEG: 8.92%	FALSE: 26.77%	NEG: 21.53%
	500	HIT: 95.93%	MISS: 0%	HIT: 67.44%	MISS: 4.07%	HIT: 65.70%	MISS: 5.81%
		FALSE: 4.07%	NEG: 0%	FALSE: 26.16%	NEG: 2.32%	FALSE: 20.93%	NEG: 7.55%

Indeed, a smaller amount of pixels are labeled as LOW and a larger quantity as HIGH by VALR-ML, whereas most pixels are classified as HIGH and MEDIUM by PM1 model, coherently with the previous retrievals and discussion (see Fig. 8).

Even though no validation data set is available to assess the overestimation of parametric models, it can be interesting to quantitatively evaluate the impact of Lidar-based retrievals in terms of no flight zones. To this end, we have computed these differences in terms of weighted occurrences with respect to three concentration thresholds ($\mathrm{Th}_1 = 2 \times 10^{-4}$ g/m^3, $\mathrm{Th}_2 = 2 \times 10^{-3}$ g/m^3, and $\mathrm{Th}_3 = 4 \times 10^{-3}$ g/m^3) following the ICAO regulations, as shown in Table IV. Substantially, if both techniques are above the given threshold there is a HIT, if PM1 is below and VALR-ML is below there is NEG, if PM1 is above and VALR-ML is below there is a FALSE, if PM1 is below and VALR-ML is above there is a MISS. From Table IV, it emerges that, as expected, considering less restrictive ash thresholds the HIT cases tend to decrease, the NEG and MISS cases tend to increase linearly, whereas FALSE cases grow, but for the Th_2 larger values are noted essentially due to the PM1 estimates around this Th_2 value (2×10^{-3} g/m^3).

IV. CONCLUSION

The use of a scanning Lidar located near volcanic sites may be useful to monitor volcanic activity and help drastically reduce the risks to aviation during these eruptions. The application of the VALR-ML algorithm to Lidar data allows estimating ash concentration and size class in a physically consistent framework in order to better understand the eruptive activity nature. The analyzed Etna cases, using the scanning Lidar system at visible wavelength, show that this sensor can be employed to detect the lowest ash concentration values of dispersed plumes in the atmosphere.

The proposed VALR-ML methodology can help finding the main microphysical ash features and the areas characterized by a specific mass concentration of smallest ash particles. This information may help quantify the impact that ash emissions have on aviation safety to halt flights in areas of high ash contamination (where the threshold is typically set to 2×10^{-3} g/m^3) in compliance with the ICAO. In the considered case study, the flight-interdicted area has been extended when using the proposed VALR-ML due to lower estimates of ash concentrations. Moreover, the knowledge of reliable ash concentration in the atmosphere may help better define the main eruption source parameters within ash dispersal models, thus improving our ability to forecast volcanic ash cloud aerial distribution.

The impact of using an advanced retrieval algorithm, such as VALR-ML, with respect to parametric retrieval techniques, has an appealing potential for improving ash mass concentration retrievals. The VALR-ML approach allows performing a more accurate ash concentration retrieval using several Lidar observables. If several Lidar observables are not available, the VALR-Reg model represents a physically based efficient compromise. Future work shall be devoted to assess the results presented in this paper by selecting more case studies where other Lidar data are collected or performing new measurements with the aim of testing the model.

APPENDIX
FROM SCATTERING MATRIX TO MUELLER MATRIX AND LIDAR OBSERVABLES

Electromagnetic scattering simulations can be performed in two basic and mutually related coordinate systems: the forward scatter alignment (FSA) convention and the backscatter alignment (BSA) convention [21], [49]. Given an incident field upon the target, in the FSA system, the scattered far-field is basically an outward wave from the target, whereas in the BSA system, it is a backward wave incident upon the target itself (useful for monostatic systems). The polarimetric response of a point or distributed target can be obtained by simultaneously measuring both the amplitude and phase of the scattered field using two orthogonal channels [26]. If the incident and scattered field vectors are decomposed into their horizontal (parallel) and vertical (orthogonal) components

$$\boldsymbol{E}^i = \boldsymbol{E}^i_v \hat{v}_i + \boldsymbol{E}^i_h \hat{h}_i \tag{A.1}$$

$$\boldsymbol{E}^s = \boldsymbol{E}^s_v \hat{v}_s + \boldsymbol{E}^s_h \hat{h}_s \tag{A.2}$$

the polarimetric response can be represented by the scattering matrix $\boldsymbol{S}$, which for plane wave illumination is given by [41]

$$\boldsymbol{E}^s = \frac{e^{jkr}}{r} \begin{bmatrix} S_{\mathrm{vv}} & S_{\mathrm{vh}} \\ S_{\mathrm{hv}} & S_{\mathrm{hh}} \end{bmatrix}_{\mathrm{FSA}} \boldsymbol{E}^i = \mathbf{S}_{\mathrm{FSA}} \boldsymbol{E}^i \tag{A.3}$$

where r is the distance from the sensor to the center of the distributed target and S_{pq} are called the scattering amplitudes in the FSA convention with $\mathbf{S}_{\mathrm{FSA}}$ the complex scattering matrix. In the backscattering case, reciprocity implies that $S_{\mathrm{vh}} = S_{\mathrm{hv}}$. Each complex element of the scattering matrix can be represented by [26]

$$S_{pq} = |S_{pq}| e^{j\phi_{pq}} = \sum_{n=1}^{N} |S^n_{pq}| e^{i\phi^n_{pq}} \tag{A.4}$$

with $p, q = h, v$ and where N is the total number of scatters that constitute the distributed target, each having

scattering amplitude $|S^n_{pq}|$ and phase ϕ^n_{pq}. It is possible to use a more efficient approach to represent the relationship between the scattered and incident field, based on the Stokes vector. Indeed, each complex scattering matrix (2×2) is converted to their corresponding real Mueller matrix or Stokes scattering operators (4×4). The elements of the Stokes vector are defined as

$$\boldsymbol{I} = \begin{cases} I = \left|E^i_h\right|^2 + \left|E^i_v\right|^2 \\ Q = \left|E^i_h\right|^2 - \left|E^i_v\right|^2 \\ U = -2\mathrm{Re}\left(E^{i*}_h E^i_v\right) \\ V = 2\mathrm{Im}\left(E^{i*}_h E^i_v\right). \end{cases} \tag{A.5}$$

Physically **I** is proportional to the total power, whereas Q, U, and V contain the information about the polarization state. The modified Stokes vector representation of a polarized wave can also be introduced by defining $I_v = I + Q$ and $I_h = I - Q$ instead of I and Q, respectively.

The relationship between transmitted and scattered Stokes vectors is expressed as a function of ensemble-averaged Mueller scattering matrix $\mathbf{M}_{\mathrm{FSA}}$ (in m^2) and decreases as $1/\mathrm{r}^2$ for a mixture of particles [28], [41]

$$\boldsymbol{I}^s = \frac{1}{r^2}\mathbf{M}_{\mathrm{FSA}}\boldsymbol{I}^i. \tag{A.6}$$

A further useful definition is the normalized ensemble-averaged Mueller scattering matrix $\tilde{\boldsymbol{M}}$ or scattering phase matrix

$$\tilde{\boldsymbol{M}} = \frac{4\pi}{k_s}\mathbf{M}_{\mathrm{FSA}} \tag{A.7}$$

where all elements are averaged over the size distribution and orientation of the particle polydispersion, as shown in (3). For example, it holds

$$M_{11} = \left\langle \frac{1}{2}(|S_{\mathrm{hh}}|^2 + |S_{\mathrm{hv}}|^2 + |S_{\mathrm{vh}}|^2 + |S_{\mathrm{vv}}|^2) \right\rangle$$
$$M_{22} = \left\langle \frac{1}{2}(|S_{\mathrm{hh}}|^2 - |S_{\mathrm{hv}}|^2 - |S_{\mathrm{vh}}|^2 + |S_{\mathrm{vv}}|^2) \right\rangle$$

with the angle brackets standing for the ensemble average. The elements of the ensemble-average Mueller matrix $\mathbf{M}_{\mathrm{FSA}}$ are quantities given in terms of the elements of the scattering matrix $\mathbf{S}_{\mathrm{FSA}}$:

It is noted that the reciprocity relation, which is a manifestation of the symmetry of the scattering process with respect to an inversion of time [28], satisfies the condition $S_{\mathrm{hv}} = S_{\mathrm{vh}}$ in FSA convention and $S_{\mathrm{hv}} = -S_{\mathrm{vh}}$ in BSA. The Mueller matrix of a distributed target of partially oriented particles, for which S_{hv} is uncorrelated with S_{vv} and S_{hh} contains only eight nonzero elements [41]

$$\mathbf{M}_{\mathrm{FSA}} = \begin{bmatrix} M_{11} & M_{12} & 0 & 0 \\ M_{21} & M_{22} & 0 & 0 \\ 0 & 0 & M_{33} & M_{34} \\ 0 & 0 & M_{43} & M_{44} \end{bmatrix}. \tag{A.8}$$

For randomly oriented particles, the scattering medium is macroscopically isotropic and mirror symmetric with respect to any plane, and in backward direction ($\theta = 180°$). This implies the following conditions in (A.8):

$$M_{44}(180°) = M_{11}(180°) - 2M_{22}(180°)$$
$$M_{33}(180°) = -M_{22}(180°)$$
$$M_{12}(180°) = M_{21}(180°) = M_{34}(180°) = 0.$$

For elastic Lidar applications, it is usual to define the backscattering coefficients (in $\mathrm{km}^{-1}\ \mathrm{sr}^{-1}$), co-polar and cross-polar, defined as combination of the elements of $\mathbf{M}_{\mathrm{FSA}}$ as (see [10], [24], [26])

$$\beta_{\mathrm{hh}} = \langle 4\pi |S_{\mathrm{hh}}|^2 \rangle = \left\langle \frac{2\pi\ (M_{11} - M_{12} - M_{21} + M_{22})}{10^3} \right\rangle$$
$$\beta_{\mathrm{vv}} = \langle 4\pi |S_{\mathrm{vv}}|^2 \rangle = \left\langle \frac{2\pi (M_{11} + M_{12} + M_{21} + M_{22})}{10^3} \right\rangle$$
$$\beta_{hv} = \langle 4\pi |S_{hv}|^2 \rangle = \left\langle \frac{2\pi (M_{11} + M_{12} - M_{21} - M_{22})}{10^3} \right\rangle. \tag{A.9}$$

The Lidar linear cross-polarization ratio and co-polarization are defined, respectively, as

$$\delta_{\mathrm{cr}} = \frac{\beta_{\mathrm{hv}}}{\beta_{\mathrm{hh}}} = \frac{\langle M_{11} + M_{12} - M_{21} - M_{22} \rangle}{\langle M_{11} - M_{12} - M_{21} + M_{22} \rangle}$$
$$\delta_{co} = \frac{\beta_{\mathrm{vv}} - \beta_{\mathrm{hh}}}{\beta_{\mathrm{vv}} + \beta_{\mathrm{hh}}} = \frac{\langle M_{12} + M_{21} \rangle}{\langle M_{11} + M_{22} \rangle}. \tag{A.10}$$

It is noted that in the case of randomly oriented particles $M_{12} = M_{21} = 0$ so that the expression of δ_{cr} is equal to the ratio of the copolar elements only of the Mueller matrix, as shown in (5) and (6). The Lidar ratio, defined in (7), is expressed as a function of the single-scattering albedo w_0 and M_{11}

$$R_{\beta\alpha} = \frac{w_0 M_{11}}{4\pi} \tag{A.11}$$

where

$$w_0 = \frac{k_s}{k_e} = \frac{M_{11}}{k_e} \tag{A.12}$$

being k_s and k_e the scattering and extinction coefficients (in km^{-1}), respectively, of the particle ensemble, the latter expressed by the extinction theorem

$$k_e = \frac{4\pi}{k_0}\langle \mathrm{Im}\{M_{11}\} + \mathrm{Im}\{M_{22}\} \rangle.$$

Note that, in analogy to Lidar, for radar applications several similar observables can be defined such as the radar volumetric co-polar reflectivity (in $\mathrm{m}^2 \cdot \mathrm{m}^{-3}$) at horizontal and vertical polarizations [49]

$$\eta_{\mathrm{hh}} = \left\langle 4\pi \frac{1}{2}(M_{11} - M_{12} - M_{21} + M_{22}) \right\rangle$$
$$\eta_{\mathrm{vv}} = \left\langle 4\pi \frac{1}{2}(M_{11} + M_{12} + M_{21} + M_{22}) \right\rangle \tag{A.13}$$

where the elements of the Mueller matrix are, indeed, typically expressed in BSA convention. The volumetric cross-polar reflectivity (in $\mathrm{m}^2 \cdot \mathrm{m}^{-3}$) is defined as

$$\eta_{\mathrm{hv}} = \left\langle 4\pi \frac{1}{2}(M_{11} + M_{12} - M_{21} - M_{22}) \right\rangle. \tag{A.14}$$

The radar reflectivity factor (in dBZ if the reflectivity is in $\mathrm{mm}^6 \cdot \mathrm{m}^{-3}$) is defined as

$$Z_{xy} = 10\log_{10}\frac{\lambda^2 2\pi}{\pi^5|K_p|^2}\eta_{xy} \tag{A.15}$$

where K_p is a dielectric factor and η_{xy} is expressed in $\mathrm{mm}^6 \cdot \mathrm{m}^{-3}$. The differential reflectivity (in decibel) and linear depolarization ratio (in decibel) can also be defined as

$$Z_{\mathrm{dr}} = 10\log_{10}\frac{\eta_{\mathrm{hh}}}{\eta_{\mathrm{vv}}}$$
$$L_{\mathrm{dr}} = 10\log_{10}\frac{\eta_{\mathrm{vh}}}{\eta_{\mathrm{hh}}}. \tag{A.16}$$

References

[1] P. Armienti, G. Macedonio, and M. T. Pareschi, "A numerical model for simulation of tephra transport and deposition: Applications to May 18, 1980, Mount St. Helens eruption," *J. Geophys. Res.*, vol. 93, no. B6, pp. 6463–6476, 1988.

[2] A. Ansmann *et al.*, "Ash and fine-mode particle mass profiles from EARLINET-AERONET observations over central Europe after the eruptions of the Eyjafjallajökull volcano in 2010," *J. Geophys. Res.*, vol. 116, p. D00U02, Oct. 2011, doi: 10.1029/2010JD015567.

[3] J. G. C. Ball, B. E. Reed, R. G. Grainger, D. M. Peters, T. A. Mather, and D. M. Pyle, "Measurements of the complex refractive index of volcanic ash at 450, 546.7, and 650 nm," *J. Geophys. Res. Atmos.*, vol. 120, no. 5, pp. 7747–7757, 2015, doi: 10.1002/2015JD023521.

[4] T. J. Casedevall, *Volcanic Ash and Aviation Safety: Proceedings of the First International Symposium on Volcanic Ash and Aviation Safety* (U.S. Geological Survey). Reston, VA, USA: U.S. Geological Survey, 1994, p. 2047.

[5] P. Chazette *et al.*, "Eyjafjallajökull ash concentrations derived from both lidar and modeling," *J. Geophys. Res. Atmos.*, vol. 117, p. D00U14, Oct. 2012, doi: 10.1029/2011JD015755.

[6] M. Coltelli, L. Miraglia, and S. Scollo, "Characterization of shape and terminal velocity of tephra particles erupted during the 2002 eruption of Etna volcano, Italy," *Bull. Volcanol.*, vol. 70, no. 9, pp. 1103–1112, 2008, doi: 10.1007/s00445-007-0192-8.

[7] J. A. Ferguson and D. H. Stephens, "Algorithm for inverting lidar returns," *Appl. Opt.*, vol. 22, no. 23, pp. 3673–3675, 1983.

[8] F. G. Fernald, "Analysis of atmospheric lidar observations: Some comments," *Appl. Opt.*, vol. 23, no. 5, pp. 652–653, 1984.

[9] V. Freudenthaler *et al.*, "Depolarization ratio profiling at several wavelengths in pure Saharan dust during SAMUM 2006," *Tellus B*, vol. 61, no. 1, pp. 165–179, 2009.

[10] J. Gasteiger, S. Groß, V. Freudenthaler, and M. Wiegner, "Volcanic ash from Iceland over Munich: Mass concentration retrieved from ground-based remote sensing measurements," *Atmos. Chem. Phys.*, vol. 11, pp. 2209–2223, Mar. 2011.

[11] R. Gertisser *et al.*, "Ignimbrite stratigraphy and chronology on Terceira Island, Azores," in *Stratigraphy and Geology of Volcanic Areas* (Geological Society of America Special Paper), vol. 464, C. Groppelli and L. Viereck-Goette, Eds. Boulder, CO, USA: Geological Society America, 2010, pp. 133–154, doi: 10.1130/2010.2464(07).

[12] G. P. Gobbi, F. Congeduti, and A. Adriani, "Early stratospheric effects of the Pinatubo eruption," *Geophys. Res. Lett.*, vol. 19, no. 10, pp. 997–1000, 1992.

[13] S. Groß, V. Freudenthaler, M. Wiegner, J. Gasteiger, A. Geiß, and F. Schnell, "Dual-wavelength linear depolarization ratio of volcanic aerosols: Lidar measurements of the Eyjafjallajökull plume over Maisach, Germany," *Atmos. Environ.*, vol. 48, pp. 85–96, Mar. 2012, doi: 10.1016./j.atmosenv.2011.06.017.

[14] J. D. Klett, "Stable analytical inversion solution for processing lidar returns," *Appl. Opt.*, vol. 20, no. 2, pp. 211–220, 1981.

[15] J. D. Klett, "Lidar inversion with variable backscatter/extinction ratios," *Appl. Opt.*, vol. 24, no. 11, pp. 1638–1643, 1985.

[16] F. S. Marzano, L. Mereu, M. Montopoli, D. Cimini, and G. Martucci, "Volcanic Ash Cloud Observation using Ground-based Ka-band Radar and Near-Infrared Lidar Ceilometer during the Eyjafjallajökull eruption," *Ann. Geophys.*, vol. 57, 2014. [Online]. Available: https://doi.org/10.4401/ag-6634

[17] F. S. Marzano, E. Picciotti, G. Vulpiani, and M. Montopoli, "Synthetic signatures of volcanic ash cloud particles from X-band dual-polarization radar," *IEEE Trans. Geosci. Remote Sens.*, vol. 50, no. 1, pp. 193–211, Jan. 2011.

[18] T. A. Mather, D. M. Pyle, and C. Oppenheimer, "Tropospheric volcanic aerosol," in *Volcanism and the Earth's Atmosphere* (Geophysical Monograph Series), vol. 139. Washington, DC, USA: AGU, 2003, pp. 189–212.

[19] L. Mereu, F. S. Marzano, M. Montopoli, and C. Bonadonna, "Exploiting microwave scanning radar for monitoring Icelandic volcanic eruption source parameters," in *Proc. 11th Eur. Radar Conf. (EuRAD)*, Oct. 2014, pp. 205–208, doi: 10.1109/.EuRAD.2014.6991243.

[20] I. M. Mishchenko and L. D. Travis, "T-matrix computations of light scattering by large spheroidal particles," *Opt. Commun.*, vol. 109, pp. 16–21, Jun. 1994.

[21] D. Pieri, C. Ma, J. J. Simpson, G. Hufford, T. Grindle, and C. Grove, "Analyses of in-situ airborne volcanic ash from the February 2000 eruption of Hekla Volcano, Iceland," *Geophys. Res. Lett.*, vol. 29, no. 16, pp. 19-1–19-4, 2002.

[22] G. Pisani *et al.*, "Lidar depolarization measurement of fresh volcanic ash from Mt. Etna, Italy," *Atmos. Environ.*, vol. 62, pp. 34–40, Dec. 2012.

[23] C. M. Riley, W. I. Rose, and G. J. S. Bluth, "Quantitative shape measurements of distal volcanic ash," *J. Geophys. Res.*, vol. 108, no. B10, pp. 2504–2514, 2003.

[24] C. Rolf, M. Krämer, C. Schiller, M. Hildebrandt, and M. Riese, "Lidar observation and model simulation of a volcanic-ash-induced cirrus cloud during the Eyjafjallajökull eruption," *Atmos. Chem. Phys.*, vol. 12, no. 21, pp. 10281–10294, 2012, doi: 10.5194/acp-12-10281-2012.

[25] W. I. Rose and A. J. Durant, "Fine ash content of explosive eruptions," *J. Volcanol. Geothermal Res.*, vol. 186, pp. 32–39, Sep. 2009, doi: 10.1016/j.jvolgeores.2009.01.010.

[26] K. Sassen, *Polarization in Lidar*, C. Weitkamp, Ed. New York, NY, USA: Springer, 2005, pp. 19–42.

[27] K. Sassen, J. Zhu, P. Webley, K. Dean, and P. Cobb, "Volcanic ash plume identification using polarization lidar: Augustine eruption, Alaska," *Geophys. Res. Lett.*, vol. 34, no. 8, pp. L08803-1–L08803-4, 2007, doi: 10.1029/2006GL027237.

[28] D. S. Saxon, "Tensor scattering matrix for the electromagnetic field," *Phys. Rev.*, vol. 100, pp. 1771–1775, Dec. 1995.

[29] U. Schumann *et al.*, "Airborne observations of the Eyjafjalla volcano ash cloud over Europe during air space closure in April and May 2010," *Atmos. Chem. Phys.*, vol. 11, no. 5, pp. 2245–2279, 2011.

[30] S. Scollo *et al.*, "Volcanic ash concentration during the 12 August 2011 Etna eruption," *Geophys. Res. Lett.*, vol. 42, no. 8, pp. 2634–2641, 2015, doi: 10.1002/2015GL063027.

[31] S. Scollo, M. Coltelli, F. Prodi, S. Folegani, and S. Natali, "Terminal settling velocity measurements of volcanic ash during the 2002–2003 Etna eruption by an X-band microwave rain gauge disdrometer," *Geophys. Res. Lett.*, vol. 32, no. 10, pp. L10302-1–L10302-5, 2005, doi: 10.1029/2004-GL022100.

[32] S. Scollo, M. Prestifilippo, G. Spata, M. D'Agostino, and M. Coltelli, "Monitoring and forecasting Etna volcanic plume," *Nat. Hazards Earth Syst. Sci.*, vol. 9, pp. 1573–1585, Sep. 2009.

[33] S. Scollo *et al.*, "Monitoring Etna volcanic plumes using a scanning LiDAR," *Bull. Volcanol.*, vol. 74, no. 10, pp. 2383–2395, 2012, doi: 10.1007/s00445-012-0669-y.

[34] C. Searcy, K. Dean, and W. Stringer, "PUFF: A high-resolution volcanic ash tracking model," *J. Volcanol. Geothermal Res.*, vol. 80, pp. 1–16, Jan. 1998.

[35] E. P. Shettle and R. W. Fenn, "Models for the aerosols of the lower atmosphere and the effects of humidity variations on their optical properties," Tech. Rep. AFGL-TR-79-0214, Sep. 1979.

[36] M. Sicard *et al.*, "Monitoring of the Eyjafjallajökull volcanic aerosol plume over the Iberian Peninsula by means of four EARLINET lidar stations," *Atmos. Chem. Phys.*, vol. 12, no. 6, pp. 3115–3130, 2012.

[37] R. S. J. Sparks *et al.*, *Volcanic Plumes*. New York, NY, USA: Wiley, 1997, p. 574.

[38] H. L. Tanaka and K. Yamamoto, "Numerical simulation of volcanic plume dispersal from Usu Volcano in Japan on 31 March 2000 using PUFF model," *Earth Planets Space*, vol. 54, pp. 743–752, Jun. 2002.

[39] M. Tesche *et al.*, "Vertically resolved separation of dust and smoke over Cape Verde using multiwavelength Raman and polarization lidars during Saharan Mineral dust experiment 2008," *J. Geophys. Res., Atmos.*, vol. 114, p. D13202, Jul. 2009, doi: 10.1029/2009JD011862.

[40] F. T. Ulaby, K. Sarabandi, and A. Nashashibi, "Statistical properties off the mueller matrix off distributed targets," *IEE Proceedings F, Radar Signal Process.*, vol. 139, no. 2, pp. 136–146, Apr. 1992.

[41] M. Wiegner, J. Gasteiger, S. Groß, F. Schnell, V. Freudenthaler, and R. Forkel, "Characterization of the Eyjafjallajökull ash-plume: Potential of lidar remote sensing," *Phys. Chem. Earth, A/B/C*, vols. 45–46, pp. 79–86, 2012. [Online]. Available: https://doi.org/10.1016/j.pce.2011.01.006

[42] D. M. Winker and M. T. Osborn, "Preliminary analysis of observations of the Pinatubo volcanic plume with a polarization-sensitive lidar," *Geophys. Res. Lett.*, vol. 19, no. 2, pp. 171–174, 1992.

[43] K. H. Wohletz, M. F. Sheridan, and W. K. Brown, "Particle size distributions and the sequential fragmentation/transport theory applied to volcanic ash," *J. Geophys. Res.*, vol. 94, no. B11, pp. 15703–15721, 1989, doi: 10.1029/JB094iB11p15703.

[44] G. Pappalardo *et al.*, "Four-dimensional distribution of the 2010 Eyjafjallajökull volcanic cloud over Europe observed by EARLINET," *Atmos. Chem. Phys.*, vol. 13, no. 8, pp. 4429–4450, 2013, doi: 10.5194/acp-13-4429-2013.

[45] D. M. Winker, "Accounting for multiple scattering in retrievals from space lidar," *Proc. SPIE*, vol. 5059, pp. 128–140, Apr. 2003.

[46] L. R. Bissonnette, "Lidar and multiple scattering," in *Lidar: Range-Resolved Optical Remote Sensing of the Atmosphere*, C. Weitkamp, Ed. New York, NY, USA: Springer, 2005, pp. 43–103.

[47] S. Mori and F. S. Marzano, "Microphysical characterization of free space optical link due to hydrometeor and fog effects," *Appl. Opt.*, vol. 54, no. 22, pp. 6787–6803, Aug. 2015.

[48] G. Pappalardo *et al.*, "EARLINET: Towards an advanced sustainable European aerosol lidar network," *Atmos. Meas. Tech.*, vol. 7, no. 8, pp. 2389–2409, doi: 10.5194/amt-7-2389-2014.

[49] V. N. Bringi and V. Chandrasekar, *Polarimetric Doppler Weather Radar*. Cambridge, U.K.: Cambridge Univ. Press, 2004.

[50] D. J. Wielaard, M. I. Mishchenko, A. Macke, and B. E. Carlson, "Improved T-matrix computations for large, nonabsorbing and weakly absorbing nonspherical particles and comparison with geometrical-optics approximation," *Appl. Opt.*, vol. 36, no. 18, pp. 4305–4313, 1997.

Luigi Mereu received the M.Sc. degree in telecommunication engineering and the Ph.D. degree in remote sensing, from the Sapienza University of Rome, Rome, Italy, in 2012 and 2016, respectively.

In 2012, he joined the Department of Information Engineering, Sapienza University of Rome, and the Centre of Excellence CETEMPS, L'Aquila, Italy, to cooperate on radar remote sensing of volcanic ash clouds within the ICT Ph.D. Program. He was a Visiting Student at the Icelandic Meteorological Office, Reykjavik, Iceland, in 2014, and at the Istituto Nazionale di Geofisica e Vulcanologia-Osservatorio Etneo, Catania, Italy, in 2015. He was involved in the FUTUREVOLC European Project in 2012 and the Aphorism European Project in 2014. He is involved in the EUROVOLC European Project in 2017. His research interests include the analysis and modeling of eruptive plume using different remote sensing systems.

Dr. Mereu was a recipient of the IEEE GRS South Italy Award for the Best Master Thesis in remote sensing in 2012.

Simona Scollo received the M.Sc. degree (Hons.) in physics from the University of Catania, Catania, Italy, in 2002, and the Ph.D. degree in physical modeling for environmental protection from the Università Alma Mater Studiorum of Bologna, Bologna, Italy, in 2006.

She joined the University of Geneva, Geneva, Switzerland, as a Visiting Scientist in 2015, the Dipartimento of di Fisica, Università di Federico II, Naples, Italy, in 2011, the Jet Propulsion Laboratory, Pasadena, CA, USA, in 2010, the Barcelona Supercomputer Center, Barcelona, Spain, in 2008, the Joint Research Centre, Ispra, Italy, in 2005, and the Department of Geology and Geophysics School of Ocean and Earth Science and Technology, Manoa, Hawaii, in 2003 and 2005. She is currently a Researcher with the Istituto Nazionale di Geofisica e Vulcanologia, Osservatorio Etneo, Catania. She has authored 35 papers in refereed international journals, over 80 presentations at international conferences and workshops. Her research interests include the analysis of the dispersal and fallout processes of eruptive plumes during explosive eruptions; calibration, sensitivity analysis and uncertainty estimation of ash dispersal models; laboratory and field experiments; development of a multidisciplinary system for the detection and monitoring of volcanic plumes; and analysis of explosive activity using different remote sensing techniques (e.g., radar, Lidar, and satellites).

Dr. Scollo was a recipient of the Rittmann Medal for young researchers in volcanology in 2011 and the paper Scollo *et al.* (2010) was selected for the "AGU Research Spotlight" in 2010. She was an Editor of a Special Issue in *Atmospheric Emissions* from Volcanoes, Scientific Committee for FisMat 2015, and a Co-Convenor and the Chairman in different sessions of EGU and IUGG. She is currently the Referee for several international journals. She coordinated several projects and one of them, the VAMOS SEGURO project, was selected in 2012 as a "best practice" among several European Cooperation Projects.

Saverio Mori (S'05–M'10) received the M.Sc. degree in telecommunications engineering from the University of Florence, Florence, Italy, in 2005, and the Ph.D. degree in remote sensing of environment from the University of Basilicata, Potenza, Italy, and from the University of Rome "La Sapienza," Rome, Italy, in 2011, through a joint program.

In 2011, he joined the Satellite Remote Sensing Laboratory, University of Florence. Since 2007, he has been a Research Scientist with CETEMPS, University of L'Aquila, L'Aquila, Italy, and with the Department of Information Engineering, Electronics and Telecommunications, Sapienza University of Rome, Rome, Italy. His research interests include analysis and modeling of atmospheric effects on space borne synthetic aperture radar response and on optical propagation along terrestrial links, radiative transfer modeling of scattering media, and radar meteorology.

Dr. Mori was a recipient of the award for the five best Italian degree theses in remote sensing from the IEEE Geoscience and Remote Sensing Society, South Italy Chapter, in 2006.

Antonella Boselli received the M.Sc. degree in physics from the University of Naples "FedericoII," Naples, Italy, in 1994.

She has been a Permanent Researcher with the Institute of Methodologies for Environmental Analysis, National Research Council, Potenza, Italy, since 2001. She was involved in developing several advanced laser remote-sensing systems (LIDAR) systems using different spectral regions from UV to IR. She has authored or co-authored over 30 papers in refereed international journals. She has participated in several national and international projects. Her research interests include the chemical and physical characterization of the atmosphere with LIDAR, and optical and microphysical characterization of atmospheric aerosol, also rising from large-scale transport phenomena, with particular reference to Saharan dust and volcanic ash transport events, analysis of multiple scattering processes and depolarization effects on LIDAR signals, validation of satellite data with LIDAR data and their integration with model results, and *in situ* measurement.

Giuseppe Leto received the M.Sc. degree in physics and the Ph.D. degree from the University of Catania, Catania, Italy, in 1990 and 1995, respectively.

From 1995 to 1999, he was a Researcher with Italian CNR, Rome, and with the Radio astronomy Institute, Noto, Italy. From 1998 to 1999, he was a Visiting Astronomer at the Center for Astrophysics and Space Astronomy, Colorado University at Boulder, Boulder, CO, USA. In 1999, he was appointed as an Astronomer at the Catania Astrophysical Observatory, Italian National Institute for Astrophysics, Catania. Since 2006, he has been responsible for the INAF "M. G. Fracastoro" Observatory located on Mount Etna. He has experienced in laboratory research on materials of interest for astrophysics, observational astronomy, computational astronomy, coordination of teams and observing facilities; he has also been a Tutor for bachelor's and Ph.D. theses and young astronomer grants. He has been part of a number of projects funded by MIUR, ASI, and EC; among them VAMOS SEGURO (VS), a "best practice" EC project oriented to test a Lidar on Etna plumes. In VS, he served as INAF-PI. He has authored over 150 papers, 80 of them in refereed international journals.

Dr. Leto was selected by the Italian Space Agency, Rome, Italy, for a Post-Doctorate Grant in "Research in Infrared Astronomy" in 1994.

Frank S. Marzano (S'89–M'99–SM'03–F'16) received the M.Sc. degree (Hons.) in electrical engineering and the Ph.D. degree in applied electromagnetics from the University of Rome "La Sapienza," Rome, Italy, in 1988 and 1993, respectively.

In 1992, he joined Florida State University, Tallahassee, FL, USA, as a Visiting Scientist. In 1993, he collaborated with the Institute of Atmospheric Physics, National Council of Research, Rome. From 1994 to 1996, he was a Post-Doctoral Researcher with Italian Space Agency, Rome.. He was a Lecturer at the University of Perugia, Perugia, Italy. In 1997, he joined the Department of Electrical Engineering, University of L'Aquila, L'Aquila, Italy, teaching courses on electromagnetic fields. In 1999, he joined the Naval Research Laboratory, Monterey, CA, USA, as a Visiting Scientist. In 2002, he became an Associate Professor and has co-founded the Center of Excellence on Remote Sensing and Hydro-Meteorological Modeling, L'Aquila. In 2005, he joined the Department of Information Engineering, Electronics and Telecommunications, Sapienza University of Rome, Rome, where he currently teaches courses on antennas, propagation and remote sensing. Since 2007, he has been the Vice Director with CETEMPS, University of L'Aquila, where he was a nominated Director in 2013. He has authored over 130 papers in refereed international journals, over 30 contributions to international book chapters, and over 300 extended abstracts on international and national congress proceedings. His research interests include passive and active remote sensing of the atmosphere from ground-based, airborne, and space borne platforms and electromagnetic propagation studies.

Dr. Marzano has been a fellow of the Royal Meteorological Society since 2012. He was an Editor of two books. From 2004 to 2014, he was an Associated Editor of the IEEE GEOSCIENCE REMOTE SENSING LETTERS and has been for the IEEE TRANSACTIONS ON GEOSCIENCE AND REMOTE SENSING (TGRS) since 2014. In 2005 and 2007, he was a Guest Co-Editor of the MicroRad04 and the MicroRad06 Special Issues for the IEEE TGRS. Since 2011, he has been an Associate Editor of the *Journal EGU Atmospheric Measurements Techniques*.